



HAL
open science

Co-variations of climate and silicate weathering in the Nile Basin during the Late Pleistocene

Luc Bastian, Carlo Mogni, Nathalie Vigier, Germain Bayon, Henry Lamb, Delphine Bosch, Marie-Emmanuelle Kerros, Christophe Colin, Marie Revel

► **To cite this version:**

Luc Bastian, Carlo Mogni, Nathalie Vigier, Germain Bayon, Henry Lamb, et al.. Co-variations of climate and silicate weathering in the Nile Basin during the Late Pleistocene. *Quaternary Science Reviews*, 2021, 264, pp.107012. 10.1016/j.quascirev.2021.107012 . hal-03405906

HAL Id: hal-03405906

<https://hal.science/hal-03405906v1>

Submitted on 27 Oct 2021

HAL is a multi-disciplinary open access archive for the deposit and dissemination of scientific research documents, whether they are published or not. The documents may come from teaching and research institutions in France or abroad, or from public or private research centers.

L'archive ouverte pluridisciplinaire **HAL**, est destinée au dépôt et à la diffusion de documents scientifiques de niveau recherche, publiés ou non, émanant des établissements d'enseignement et de recherche français ou étrangers, des laboratoires publics ou privés.

Co-variations of climate and silicate weathering in the Nile Basin during the Late Pleistocene

Luc Bastian^{1,2*} & Carlo Mogni^{1,3*†}, Nathalie Vigier², Germain Bayon⁴, Henry Lamb^{5, 6},
Delphine Bosch⁷, Marie-Emmanuelle Kerros², Christophe Colin⁸, Marie Revel¹

*co-1st authors

†corresponding author: mogni@geoazur.unice.fr

¹ Université de la Côte d'Azur, CNRS, OCA, IRD, Geoazur, 250 rue Albert Einstein, 06500 Valbonne, France

² Laboratoire d'Océanographie de Villefranche sur Mer (LOV, IMEV), CNRS, Sorbonne Université, 181 chemin du Lazaret, 06320, Villefranche sur Mer, France

³ Université Côte d'Azur, Centre National de la Recherche Scientifique (CNRS), Cultures et Environnements. Préhistoire, Antiquité, Moyen Age (CEPAM) – UMR 7264, 24 av. des Diables Bleus 06300 Nice, France

⁴ IFREMER, Unité de Recherche Géosciences Marines, 29280 Plouzané, France

⁵ Department of Geography and Earth Sciences, Aberystwyth University, Aberystwyth SY23 3 DB, UK

⁶ Botany Department, School of Natural Sciences, Trinity College, Dublin 2, Ireland

⁷ Géosciences Montpellier, UMR-CNRS 5243, Université de Montpellier, 34095 Montpellier, France

⁸ Laboratoire GEOsciences Paris-Sud (GEOPS), UMR 8148, CNRS-Université de Paris-Sud, Université Paris-Saclay, Bâtiment 504, 91405 Orsay Cedex, France.

27 **Abstract**

28

29 We have investigated provenance and weathering proxies of the clay-size sediment exported
30 from the Nile River basin over the last 110,000 years. Using neodymium isotope composition
31 of sediments from both the Nile Deep Sea-Fan and Lake Tana, we show that the Nile River
32 branches draining the Ethiopian Highlands have remained the main contributors of clays to
33 the Nile delta during the Late Quaternary. We demonstrate that fluctuations of clay-size
34 particle contribution to the Nile Delta are mainly driven by orbital precession cycle, which
35 controls summer insolation and consequently the African monsoon intensity changes. Our
36 results indicate that - over the last 110,000 years – the proportion of clays coming from
37 Ethiopian Traps fluctuates accordingly to the intensity of the last 5 precession cycles (MIS 5
38 to MIS 1). However, there is a threshold effect in the transport efficiency during the lowest
39 insolation minima (arid periods), in particular during the MIS3. Several arid events
40 corresponding to the Heinrich Stadial periods are associated with small or negligible clay
41 source changes while chemical weathering proxies, such as $\delta^7\text{Li}$, Mg/Ti and K/Ti, vary
42 significantly. This suggests a straightforward control of weathering by hydro-climate changes
43 over centennial to millennial timescales. Our data also suggests a significant but more
44 progressive influence of the temperature decrease between 110kyr and 20kyr. Taken
45 altogether, the observed tight coupling between past climate variations and silicate weathering
46 proxies leads us to conclude that precipitation changes in northeast Africa can impact soil
47 development over a few hundred years only, while the influence of temperature appears more
48 gradual.

49

50

51

52 **1. Introduction**

53 Monsoons are the dominant seasonal mode of climate variability in the tropics, acting as
54 important conveyors of atmospheric moisture and energy at the global scale (Mohtadi et al.,
55 2016). In north-East Africa, the onset of Late Quaternary humid periods has been attributed to
56 the northward migration of the rain belt associated with the Inter Tropical Convergence Zone
57 (ITCZ) in relation with precession-driven insolation changes as well as the Congo Air
58 Boundary (CAB; Demenocal et al., 2000; Gasse, 2000; Rossignol-Strick et al., 1982;
59 Skonieczny et al., 2019, Tierney et al., 2010; Junginger et al., 2014). The last period of more
60 intense rainfall compared to present, the so-called African Humid Period (AHP), occurred
61 between ~14 and ~6 kyrs cal. BP (e.g. Costa et al., 2014; Demenocal et al., 2000; Shanahan et
62 al., 2015). These past humid periods were characterized by enhanced freshwater discharge
63 and sediment export from the large African river systems to surrounding ocean margins
64 (Blanchet et al., 2021; Mologni et al., 2020; Skonieczny et al., 2015). A number of recent
65 studies conducted at a high temporal resolution (10–1000 years) in lake and deltaic
66 sedimentary records across northern Africa suggested that gradual long-term monsoon
67 oscillations had been often punctuated by millennial-scale episodes of hyperaridity (Bastian et
68 al., 2017; Berke et al., 2012; Blanchet et al., 2020; Castañeda et al., 2016; Collins et al., 2013;
69 Costa et al., 2014; Foerster et al., 2012; Liu et al., 2017; Tierney et al., 2013, 2011b, 2011a,
70 2008; Verschuren and Russell, 2009), as exemplified by significant increase in aeolian dust
71 deposition in sediment records from African margins (Bouimetarhan et al., 2012; Collins et
72 al., 2017, 2013; Heinrich et al., 2021; McGee et al., 2013; Tierney et al., 2017). These
73 hyperarid episodes occurred contemporaneously with North Hemisphere cooling events
74 recorded in Greenland ice cores (i.e. Greenland stadials; Dansgaard et al., 1993) and in North
75 Atlantic sediment cores (Heinrich Stadials; Bond et al., 1993; Heinrich, 1988). Up to now,
76 over the tropics, these events were mainly described through the use of organic biomarkers

77 and bulk sediment geochemical tracers (δD_{wax} , Ti/Ca ratio; Castañeda et al., 2016; Collins et
78 al., 2017; Tierney et al., 2008; Tierney and DeMenocal, 2013). There is still debate about the
79 exact mechanisms that would explain these short-term hydroclimate changes (orbital forcing
80 and/or internal hemispheric versus nonlinear biogeophysical feedbacks processes; e.g. Collins
81 et al., 2017, 2011).

82 Sediment deposition in deltas is usually dominated by the export of terrigenous material
83 delivered from flooded rivers, highly sensitive to changes in precipitation rates and land cover
84 in corresponding drainage basins (Macklin et al., 2012). The sediment records preserved at
85 the Nile Deep-Sea Fan (NDSF) provide suitable archives for reconstructing past climate
86 variations at a high temporal resolution (100 to 1000 years) in north-East Africa (Almogi-
87 Labin et al., 2009; Bastian et al., 2017; Blanchet et al., 2013; Costa et al., 2014; Hamann et
88 al., 2009; Hennekam et al., 2015; Mologni et al., 2020; Revel et al., 2015; Weldeab et al.,
89 2014). Currently, about 95% of the terrigenous material deposited at the Nile deep-sea fan is
90 derived from the Ethiopian Highlands (Garzanti et al., 2015; Padoan et al., 2011). A close link
91 between precipitation and physical erosion in the Nile River basin has already been
92 demonstrated for the Late Pleistocene period (e.g. Blanchet et al., 2014). Past humid periods
93 were systematically accompanied by accelerated deposition of iron/smectite-rich sediments,
94 reflecting enhanced physical erosion and transport processes from the Ethiopian Highlands
95 (Blanchet et al., 2014; Krom et al., 2002, 1999; Langgut et al., 2011; Revel et al., 2015, 2014,
96 2010, Ehrmann et al., 2016).

97 In contrast, only a few studies have investigated past relationships between climate and
98 silicate weathering on continents over the Quaternary period (Yang et al. 2020; Bastian et al.,
99 2017; Bayon et al., 2012; Beaulieu et al., 2012; Clift et al., 2020, 2014; Dosseto et al., 2015;
100 Limmer et al., 2012; Pogge von Strandmann et al., 2017). To date, there is no consensus on
101 both the magnitude and the timing of chemical weathering response to rapid climate changes.

102 During the last two decades, lithium isotopes (conventionally expressed as $\delta^7\text{Li}$) have been
103 explored as tracers of silicate weathering in both modern and ancient environments (Bastian et
104 al., 2017; Dellinger et al., 2014, 2015, 2017; Huh et al., 1998; Philip A.E. Pogge von
105 Strandmann et al., 2017; Pogge von Strandmann et al., 2010, 2020; Vigier et al., 2009).
106 During weathering, mass-dependent isotope fractionation results in significant enrichment of
107 the lighter lithium isotope (^6Li) into secondary mineral phases such as clays (Dupuis et al.,
108 2017; Li and West, 2014; Pistiner and Henderson, 2003; Vigier et al., 2008; Wimpenny et al.,
109 2010; Hindshaw et al., 2019). As reported or modeled in Bastian et al. (2017), Bouchez et al.
110 (2013), Pogge von Strandmann et al. (2017, 2010), Misra and Froelich (2012), water or clay
111 $\delta^7\text{Li}$ values primarily reflect the degree of ‘incongruency’ of the continental weathering
112 process, which is a function of the dissolution vs neoformation rate. Indeed, the proportion of
113 - isotopically fractionated - Li incorporated into neoformed secondary phases, compared to
114 the one released more congruently to waters during rock dissolution or mineral leaching,
115 represents the most important control of Li isotope signatures in soils and rivers. When, at the
116 basin scale, the denudation flux compensates the soil production rate, physical and chemical
117 weathering processes are considered at steady-state and the ‘incongruency ratio’ is then
118 directly related to the chemical weathering intensity (W/D, ratio of silicate chemical
119 weathering over total denudation, as defined by Bouchez et al. [2013], Caves Rügenstein et al.
120 [2019] and Dellinger et al. [2017]). Exception is made for basin with particular high W/D
121 ratios, because dissolution is so intensive that secondary minerals also release to draining
122 waters their isotopically light Li (leading to a “bell shape” trend of $\delta^7\text{Li}$ as a function of W/D,
123 see Dellinger et al., [2015]).

124 The aim of our study is to better understand the impact of monsoon-rainfall changes on both
125 erosion and weathering processes in the Nile Basin over the last 110 kyrs. Recently, Bastian et
126 al. (2017) reported $\delta^7\text{Li}$ measurements for a total of 55 clay-size sediment fractions extracted

127 from core MS27PT from the NDSF. The obtained $\delta^7\text{Li}$ data ranged between 4 ‰ and -1.2 ‰
128 displaying systematic co-variations with proxies for hydroclimate variability over the last
129 32,000 years. Additional data are now needed to investigate whether this relationship held
130 true over longer timescales. To this end, we have conducted a source-to-sink approach, which
131 aimed at comparing sediment records from both the NDSF and the Lake Tana, located at the
132 source of the Blue Nile River in the Ethiopian Highlands. Our approach combines the use of
133 geochemical and isotopic tracers of sediment provenance (Nd isotopes) and silicate
134 weathering (major elements; Li isotopes). By focusing on the finest – clay rich- size fraction
135 of the sediment ($<2\mu\text{m}$) we minimize potential complexities related to granulometric
136 processes and mineral sorting occurring during sediment transport and deposition, as
137 described in Bastian et al. (2019, 2017) for the Nile Basin. Additionally, our source-to-sink
138 approach allows us to discuss the role of continental geomorphic processes on the terrigenous
139 delivery to the Nile basin. Finally, this study includes the investigation at relatively high
140 temporal resolution of several hyper-arid millennial-scale episodes (i.e. Heinrich Stadials).

141

142 **2. Regional setting and samples**

143 **2.1. Geological and hydrology setting of the Nile River Basin**

144 The Nile River Basin (about $3.3 \times 10^6 \text{ km}^2$) extends across more than 30 degrees of latitude
145 (from 4°S to 30°N, Fig. 1). It is composed of two major sub-drainage basins characterized by
146 different lithologies, but overall dominated by silicate rocks (Ghilardi and Boraik, 2011). The
147 Ethiopian Highlands, corresponding to the Ethiopian Traps (age of ~30 Ma), is composed of
148 Cenozoic basaltic rocks. The Sobat, the Blue Nile and the Atbara rivers originate from the
149 Ethiopian Traps sources (Garzanti et al., 2015). The Central African Craton (age $> 3 \text{ Ga}$) is
150 composed of Precambrian metamorphic rocks drained by the Bahr el Jebel River (Garzanti et

151 al., 2015), which is joined by the Sobat River to form the White Nile (Williams et al., 2015).
152 Over the hydrological year, the Nile River displays a unimodal discharge patterns
153 characterized by intense floods during the summer, essentially caused by the northward
154 migration of the ITCZ, and associated monsoonal precipitation across the Ethiopian
155 Highlands (Garzanti et al., 2015). The Bahr el Jebel/White Nile is originated from the
156 equatorial uplands Uganda, Rwanda and Burundi, and in particular from the outflow of Lake
157 Victoria and Lake Albert. The contribution of the Bahr el Jebel/White Nile remains more or
158 less constant throughout the year, due to a more uniform rainfall pattern in the Equatorial
159 region with 1-2 m of rainfall distributed in two rainy seasons (Garzanti et al., 2015;
160 Nicholson, 2000).

161 Thus, the precipitation regime along the Nile catchment is mainly caused by the West
162 African monsoon, modulated by the Indian Summer Monsoon (ISM) dynamics. Over the
163 Ethiopian Highlands, precipitation is fed by moisture originating from three sources: the West
164 African Monsoon (WAM), the Indian Ocean and the Mediterranean Sea, Arabian Peninsula
165 and the Red Sea northern regions (Viste and Sorteberg, 2013). A range of 69–95% and 5–24%
166 of the total precipitation are currently derived from the Gulf of Guinea and Indian Ocean,
167 respectively (Costa et al., 2014; Verschuren et al., 2009). Runoff from the Ethiopian Traps
168 (where 1500 m to 3000 m a.s.l. elevation concentrates most precipitation) greatly contributes
169 to the lower Nile discharge and to a majority of its transported sediment (Lamb et al., 2007;
170 Williams et al., 2006).

171

172 **2.2. Geochemical characterization of detrital sediments from the Nile River Basin**

173 The NDSF has built up continuously since the Oligocene through sedimentary inputs from
174 the Nile River basin (Ducassou et al., 2009; Faccenna et al., 2019; Mascle, 2014; Migeon et

175 al., 2010; Revel et al., 2015, 2014, 2010). For the last 110,000 years, the most active part of
176 the fan has been the so-called Rosetta branch (Ducassou et al., 2009, 2008). Sedimentation
177 rates at the NDSF have varied drastically from ≈ 400 cm/kyr during humid periods such as
178 AHP, to much lower accumulation rates ($\approx 1-10$ cm/kyr) during arid periods (Ducassou et
179 al., 2008; Langgut et al., 2011; Revel et al., 2010). This reduction of particulate fluxes is in
180 line with the drying up of large lakes such as Lake Victoria, Albert, Tana situated in the Nile
181 basin system (Gasse, 2000; Lamb et al., 2007; Talbot and Lærdal, 2000; Williams et al.,
182 2006). The provenance of the sediment exported to the NDSF has been inferred from the Nd
183 and Sr radiogenic isotope compositions of mud and sand fractions from sediments in transit
184 along all major Nile branches (see map in Fig. 1; Garzanti et al., 2015; Padoan et al., 2011;
185 Talbot and Brendeland, 2001; Woodward et al., 2015). Sediment Nd isotopic compositions
186 (expressed from herein using the epsilon notation ϵNd) are not affected much by weathering
187 processes and hence faithfully reflects geographical provenance and crustal age of the
188 source rocks (Bayon et al., 2015). The Nile basin is well suited to this isotopic tracer because
189 of the contrasting ϵNd signatures characterized by the Cenozoic Ethiopian traps ($\epsilon\text{Nd} \approx 0$;
190 Fig. 1) and the Precambrian Central Africa Craton ($\epsilon\text{Nd} \approx -30$, Garzanti et al., 2015). The
191 Bahr el Jebel and Victoria-Albert Nile-derived fluvial muds are characterized by $\epsilon\text{Nd}(0) = -$
192 25 and range from -29 to -36, respectively (Padoan et al., 2011), whereas the White Nile
193 mud ϵNd is around -10, resulting from the mixture of basaltic (Ethiopian Traps) and
194 metamorphic (Precambrian Craton) rocks. The present-day White Nile contributes to
195 about 2 million tons of sediment particles to the main Nile at Khartoum, in contrast to
196 the 41 and 14 million tones provided by the Blue Nile and Atbara rivers, respectively,
197 before they were dammed (Williams et al., 2015). Thus, sediment budgets calculated by
198 integrating isotopic data on muds and sands are consistent with dominant contribution from
199 the Blue Nile and Atbara to total main Nile load, whereas the Bahr el Jebel/White Nile

200 sediment loads contribution to the main Nile are less important (Garzanti et al., 2015;
201 Padoan et al., 2011). The Sahara Desert, in particular the Libyan desert, represents another
202 source of particles to the Nile Delta with aeolian dust inputs estimated at 20 to 40 g/m²/yr
203 (Grousset et al., 1988; Krom et al., 1999). The Saharan dust contribution (Saharan
204 Metacraton sources characterized by ϵNd from -15 to -10; Abdelsalam et al., 2002; Grousset
205 et al., 1988) depends on the aridity of the region and the wind strength. Also, the Arabian-
206 Nubian Shields (ANS, Johnson et al., 2011) located along the Red Sea margin can be a
207 minor source of particle, with ϵNd from -2.5 to -0.5 (Palchan et al., 2013). Thus, Nd isotopes
208 have shown to be a powerful tool to investigate how sediment sources have changed in the
209 past, in particular during the Late Quaternary (Bastian et al., 2017; Blanchet et al., 2015,
210 2021; Castañeda et al., 2009; Revel et al., 2015; Weldeab et al., 2003). At the scale of the
211 Holocene and the last deglaciation, the highest ϵNd values recorded during the AHP, from
212 ~14 to ~8 ka BP, indicate larger proportions of particles derived from the Ethiopian Traps
213 (Bastian et al., 2017; Blanchet et al., 2014; Revel et al., 2015). Indeed, the radiogenic Nd
214 isotopic signatures ($\epsilon\text{Nd} \approx -2$) are closer to values observed in the Ethiopian Traps (ϵNd 0 to
215 7). In contrast, during more arid periods, sediment deposited at the NDSF are characterized
216 by lower ϵNd values (-8 to -12), indicating reduced sediment inputs from Ethiopian Traps,
217 together with higher relative contributions from the other sediment sources. Previous studies
218 have argued very low sediment contributions from the White Nile at present (about 3 ± 2 % of
219 the total Nile sediment discharge; Garzanti et al., 2015). This is because most of the coarse
220 grained sediment transported by the White Nile is trapped within the Sudd marshes in South
221 Sudan (Fielding et al., 2017; Garzanti et al., 2015). However, it was not always the case.
222 Indeed, during arid times, reduced Ugandan lakes overflow into Bahr el Jebel/White Nile,
223 induces the Sudd swamps drying out, favouring thus the sediment delivery at the beginning
224 of the following humid period (Williams, 2019). Additionally, water inputs of White Nile

225 may have substantially changed through the time producing marked flooding events (Talbot
226 and Lærdal, 2000; Williams, 2019; Williams et al., 2006, 2010). Thus, as proposed by
227 Blanchet et al. (2013) using granulometric measurements, the Bahr el Jebel/White Nile may
228 have represented, during the Late Pleistocene, a non-negligible source of sediments to the Nile
229 River.

230

231 **2.3. Marine sediment core MS27PT from the Nile deep-sea fan**

232 The 7.3 m long Core MS27PT (N31°47'90, E29°27'70) was collected at 1389 m water depth
233 in the NDSF during the Mediflux MIMES cruise (2004), at around 90km from the Nile
234 Rosetta River mouth. Its age model is based on 29 AMS ¹⁴C dates first published in (Bastian
235 et al., 2017; Revel et al., 2015, 2010) and on $\delta^{18}\text{O}$ stratigraphy (Revel et al., 2015, 2010; see
236 Fig. S1 and Table S1). Core MS27PT lies directly under the influence of the Nile freshwater
237 input and provides a continuous record of sediment discharge from the Nile River basin for
238 the last 110 kyr (Mologni et al., 2020; Revel et al., 2015, 2014, 2010). This is well illustrated
239 by high-resolution XRF core scanner log(Ti/Ca) ratios (Fig. 2 and S1; Bahr et al., 2015; Liu et
240 al., 2017; Revel et al., 2010), which reflect variable relative proportions of terrestrial versus
241 marine inputs. Periods of low monsoon intensity were associated with deposition of light-
242 colored sediments dominated by biogenic carbonate shells (Fig. S1), while high monsoon
243 periods usually correspond to darker -Fe-Ti rich - sediments derived from the Nile floods and
244 also from a good preservation of organic matter within Sapropel layers (De Lange et al., 2008;
245 Rohling, 1994; Rohling et al., 2015). In core MS27PT, Sapropels S4, S3 and S1 are visible
246 and associated with high Sulphur concentrations and low foraminifera $\delta^{18}\text{O}$ (Revel et al.,
247 2010), which are contemporaneous with massive freshwater discharge from the Nile River.
248 Clay fractions are continuously dominated by smectite (65 to 98 %), with illite, chlorite and
249 kaolinite in smaller proportions (Revel et al., 2015, 2010; Table S2).

250

251 **2.4. Lake sediment core 03TL3 from Lake Tana (Ethiopian Highlands)**

252 We have also analyzed ϵNd for the clay-size fractions extracted from core 03TL3, collected in
253 2003 in the central part of Lake Tana (13.8 m water depth; Lamb et al., 2007). Core 03TL3
254 covers the last 16 kyr period. Lake Tana (21°N, 37.25°E, 1830 m a.s.l.; Fig. 1) is the largest
255 lake in Ethiopia and represents, with the tributary downstream, the major source of water to
256 the Blue Nile River. The age model of this core is based on 17 AMS ^{14}C dates published by
257 Marshall et al. (2011). This sedimentary record first provides evidence for geochemical and
258 mineralogical variations related to past changes in the monsoon activity (Costa et al., 2014;
259 Lamb et al., 2007; Marshall et al., 2011). For instance, Costa et al. (2014) showed that $\delta\text{D}_{\text{wax}}$
260 (i.e. a proxy for past humidity) decreased during the African Humid Period, which was
261 interpreted as reflecting higher rainfall contributions from the Atlantic Ocean at that time.

262

263 **3. Methods**

264 **3.1. Sampling, sediment treatment and clay extraction**

265 Each sample corresponds to a 1 cm cut section along studied sediment cores. Considering
266 variations in sedimentation rates along sediment cores, this 1cm cut corresponds to a time
267 interval ranging from 10-70 years and 400-1000 years for humid and arid periods,
268 respectively.

269 The sampling for the clay-sized fraction analyses of the Nd/Li isotopes and K/Ti and Mg/Ti
270 ratios is about 2 cm for the last 31,000 years (i.e. a temporal resolution of about 1000 years).
271 For the last glacial period (75 to 25 kyr) the sampling is based on K/Al ratio variations (see

272 Fig S1) which indicates an increase in this ratio consistent with the timing of the Heinrich
273 events recorded in North Atlantic (Snoeckx et al., 1999).

274 Bulk samples (about 0.5 g) were first sieved at 63 μm and dried at 65 $^{\circ}\text{C}$. Mineralogical
275 composition of some fine-grained $<63\mu\text{m}$ sediment samples was determined by XRD Bruker
276 D5000 at the University of Strasbourg (LHYGES). Before separation of the clay fraction from
277 the $<63\mu\text{m}$ fraction, the sample was treated for carbonate removal using 1N HCl for 30 min
278 in an ultrasonic bath. Clays ($<2\mu\text{m}$) were extracted from the carbonate-free detritus by
279 physical decantation in 50 ml of ultra-pure water mixed with 60 μl of sodium
280 hexametaphosphate solution (100 mg/l).

281 The clay minerals were identified by X-ray diffraction (XRD) using a PANalytical
282 diffractometer at the GEOPS laboratory (Université Paris-Saclay, France) on oriented mounts.
283 Briefly, deflocculation was accomplished by successive washing with distilled water after
284 removing carbonate and organic matter by treating with acetic acid and hydrogen peroxide,
285 respectively. Particles smaller than 2 μm were separated by sedimentation and centrifugation.
286 Three XRD runs were performed, following air-drying, ethylene-glycol solvation for 24
287 hours, and heating at 490 $^{\circ}\text{C}$ for 2 hours. The clay minerals were identified according to the
288 position of the (001) series of basal reflections on the three XRD diagrams. Mixed layers
289 composed mainly of smectite-illite (15–17 \AA) were included in the “smectite” category. Semi-
290 quantitative estimates of peak areas of the basal reflections for the main clay mineral groups
291 of smectite (15–17 \AA), illite (10 \AA), and kaolinite/chlorite (7 \AA) were performed on the
292 glycolated curve using the MacDiff software. The relative proportions of kaolinite and
293 chlorite were determined based on the ratio from the 3.57/3.54 \AA peak areas. The replicate
294 analyses of a few selected samples gave a precision of $\pm 2\%$. Based on this XRD method, the
295 semi-quantitative evaluation of each clay mineral had an accuracy of $\sim 4\%$.

296 After drying, clays were crushed in an agate mortar and about 10 mg of this powder was
297 digested using a concentrated HF/HNO₃/HCl mixture. The solution was evaporated at low
298 temperature and the residue was completely dissolved in 1N HCl prior to Li separation
299 solid/liquid chromatography columns (Vigier et al., 2009).

300

301 **3.2. Measurement of major and trace element concentrations**

302 Major (K, Ca, Mg, Mn, Fe, Al ,Ti) and a few trace (Sr, Ba) elements were analyzed by ICP-
303 AES at the LOV. Accuracy was assessed using the certified reference material BEN and water
304 standard TM 28.4. The 2 σ errors on concentrations range between 1.6% and 3.5 % for major
305 and trace elements (more details in Bastian et al., 2017).

306

307 **3.3. Lithium isotope analyses**

308 For chemical Li purification in the LOV clean lab, a solution containing ~60 ng of lithium
309 was introduced on a cationic resin column (AG50X12) and Li was eluted using titrated
310 ultrapure 1.0 N HCl (Vigier et al., 2008). This separation was performed twice to ensure
311 perfect Li-Na separation. LiCl solution was then evaporated to dryness and re-dissolved in
312 0.05 N HNO₃ for isotope analyses. Lithium isotope analyses were performed at the Ecole
313 Normale Supérieure de Lyon (CNRS-INSU National Facilities) using a Neptune *Plus*
314 (Thermo-Fisher) multi-collector inductively coupled plasma spectrometer (MC-ICP-MS)
315 along with a sample-standard bracketing technique. A combination of Jet and X cones were
316 used, as well as an Aridus II desolvating system, resulting in a sensitivity of 1Volt ⁷Li /ppb
317 (Balter and Vigier, 2014) Li (Balter and Vigier, 2014). Before analyses, Li fractions were
318 diluted to match 5 ppb Li. Total procedural blanks were negligible (< 10 pg Li), representing
319 ~0.02% maximum of the total Li fraction for each sample. The accuracy of isotopic

320 measurements was assessed several times during each measurement session using reference
321 Li7-N solution (Carignan et al., 2007) and other reference materials (BE-N basaltic rock
322 powder and seawater). Without separation chemistry, mean $\delta^7\text{Li}$ values of $30.2\pm 0.4\%$ (2SD,
323 $n=32$) were obtained for Li7-N, which compares well with published and nominal values
324 (Carignan et al., 2007). After chemical purification, the mean values for $\delta^7\text{Li}$ were 30.3 ± 0.4
325 (2SD, $n=22$), 5.45 ± 0.2 (2SD, $n=3$) and $31.1\pm 0.3\%$ (2SD, $n=6$) for Li7-N, BE-N and seawater,
326 respectively, which also compare well with published values (Millot et al., 2004). To verify
327 the homogeneity of the clay fraction and the reproducibility of clay separation, various
328 aliquots of 5 different clay separations were also analyzed, resulting in a reproducibility of
329 0.37% (2SD; $n=14$) as previously reported in (Bastian et al., 2018, 2017).

330

331 **3.4. Neodymium isotope analyses**

332 The Nile clay Nd isotopic compositions were measured at the Pôle Spectrométrie Océan
333 (Brest, France). Neodymium was purified using conventional ion chromatography (Bayon et
334 al., 2012). Nd isotopic compositions were determined using sample-standard bracketing, by
335 analysing JNdi-1 standard solutions every two samples. Mass bias corrections were made
336 using the exponential law considering $^{146}\text{Nd}/^{144}\text{Nd} = 0.7219$. Mass-bias corrected values for
337 $^{143}\text{Nd}/^{144}\text{Nd}$ were normalized to a JNdi-1 value of $^{143}\text{Nd}/^{144}\text{Nd} = 0.512115$ (Tanaka et al.,
338 2000). Repeated analyses of bracketed JNdi-1 standard solutions during the course of this
339 study yielded $^{143}\text{Nd}/^{144}\text{Nd}$ of 0.512117 ± 0.000012 (2 SD, $n=16$), corresponding to an external
340 reproducibility of $\sim \pm 0.23\epsilon$ (2 SD).

341 Tana Lake clays have been processed at Geosciences Montpellier laboratory (University of
342 Montpellier). The chemical separation of Nd includes a first step of separation using AG50W-
343 X-8 cation exchange resin to collect rare earth elements (REE), followed by a second step to

344 purify Nd using HDEHP conditioned Teflon columns. Nd isotopes were measured using a
345 Thermo-Fischer Neptune *Plus* MC-ICP-MS from the AETE-ISO geochemistry platform
346 (OSU OREME). $^{143}\text{Nd}/^{144}\text{Nd}$ ratios were corrected from internal mass bias using an
347 exponential law and a value of 0.7219 for the $^{146}\text{Nd}/^{144}\text{Nd}$ ratio. The external mass bias was
348 corrected using standard bracketing method with two different standards (JMC321 and
349 AMES-Rennes). During the course of the study JMC-321 and AMES-Rennes (Chauvel and
350 Blichert-toft, 2001) standards yielded respectively an average of 0.511115 ± 7 (2σ , $n=8$) and
351 0.512959 ± 6 (2σ , $n=8$) for the $^{143}\text{Nd}/^{144}\text{Nd}$ ratio. Nd procedural blank was 22pg. For all
352 samples, epsilon Nd values (ϵ_{Nd}) were calculated using $^{143}\text{Nd}/^{144}\text{Nd} = 0.512638$ (Bouvier et
353 al., 2008).

354

355 **4. Results**

356 **4.1. Core MS27PT**

357 All geochemical data for core MS27PT clay fractions are presented in Tables 1 and S2. The
358 Nd isotopic composition of clay-size fractions (clay ϵ_{Nd}) varies from -7.69 to -0.98 with a
359 value of that falls down systematically to ~ -7.5 during low insolation periods. Under high
360 insolation, clay ϵ_{Nd} increases up to -4 (Fig. 2). The downcore evolution of ϵ_{Nd} is in phase
361 with $\text{Log}(\text{Ti}/\text{Ca})$ (Fig. 2) as well as with sedimentation rates (see Fig.S1). This documents
362 higher detrital sediment inputs from Ethiopian Traps during the last five high insolation
363 periods. Clay Mg/Ti and K/Ti ratios also oscillate between arid and humid periods (from ≈ 3.5
364 to 2.5 and from 2.5-3 to 1.5 respectively), with the highest values being systematically
365 associated to the lowest insolation. Overall, during the last 110,000 years, geochemical tracers
366 follow the insolation trend, hence variations in monsoon intensity in northern Africa
367 (Singarayer and Burrough, 2015; Tjallingii et al., 2008).

368 Over the last 110,000 years, clay $\delta^7\text{Li}$ values range between 1 ‰ and 4 ‰, which is the same
369 range of values already established for the last 35 kyr from the same core (Bastian et al.,
370 2017; Fig. 2). However, between 110 kyr and 35kyr, clay $\delta^7\text{Li}$ do not show the same
371 systematics with insolation as since 35 kyr (Bastian et al., 2017). The centennial to decennial
372 high resolution Ti/Ca ratio (measured on the bulk sediment every mm by XRF core scanner)
373 highlight lower values during the Younger Dryas (YD), during the five arid (low insolation)
374 periods, as well as during several short-time excursions (Fig. 2). Indeed, from 70 to 10 kyr,
375 clay $\delta^7\text{Li}$ display specific short-term increases (pointed as arrows in Fig. 2), which are
376 unrelated in terms of duration and intensity to the insolation curve. Some of these rapid
377 excursions co-vary with elemental ratios, but some do not. An additional feature of the clay
378 $\delta^7\text{Li}$ record in core MS27PT is the progressive decrease of the $\delta^7\text{Li}$ minima between 110 and
379 25 kyr BP (dotted line in Fig. 2).

380

381 **4.2. Core 03TL3 Lake Tana**

382 All data for core 03TL3 from the Lake Tana are displayed in Table 2. The ϵNd compositions
383 of all clay-size fractions yields a mean value of 2.0 ± 0.5 (2SD, $n=13$; Fig. 3), consistent with
384 the ϵNd value determined for Blue Nile river sediments by Garzanti et al., (2015) ($\epsilon\text{Nd} = 1.8$,
385 Fig. 1). $\delta^7\text{Li}$ values of clay-sized fractions from core 03TL3 range from 0.8 ‰ to 2.9 ‰ over
386 the last 16 kyr BP, with a mean value of 1.7 ‰. These values are comparable, within errors, to
387 the ones obtained in core MS27PT clays for the same period (Fig. 3).

388

389 **5. Discussion**

390 As described in the Result section, the MS27PT sediments located in NDSF first show that
391 various geochemical proxies evolve in phase with changes in the monsoonal system, which

392 are primarily controlled by precession-forced insolation variations. During the last 110 kyrs,
393 each low insolation period (to a lesser degree for the one at 45 kyrs BP), is characterized by a
394 decrease in the clay ϵNd values, and by an increase in clay Mg/Ti and K/Ti ratios (Fig. 2).

395 In addition, geochemical analyses highlight numerous short-term excursions, in particular for
396 Li isotopes, K/Ti and Mg/Ti ratios. Some of them – but not all - are accompanied by ϵNd
397 drops, similar to those as during periods of low insolation, but less intensive in magnitude.
398 These short excursions are in line with the timing of Heinrich Stadials, as determined in
399 Greenland ice core (NGrip, Andersen et al., 2004) and in North Atlantic sediments (Collins et
400 al., 2013; Hemming, 2004; see section 5.3.).

401

402 **5.1. Impact of insolation change on physical erosion and sediment transport**

403 **5.1.1. Provenance of clay fractions exported to the Nile deep-sea fan**

404 For the Nile River and other large river basins, regional paleoclimatic reconstructions are
405 generally based on the application of geochemical proxies to the bulk detrital fraction, without
406 particular grain-size separation (Costa et al., 2014; Lamb et al., 2018; Marshall et al., 2011;
407 Revel et al., 2015, 2010; Tierney et al., 2011b). While clay mineralogy has been used for
408 decades in paleoclimatic studies, the geochemistry of the finest clay-size sediment fractions
409 ($<2\mu\text{m}$) has been largely unexplored, apart from a few paleoenvironmental studies (Bastian et
410 al., 2017; Bayon et al., 2012; Blanchet et al., 2015; Chen et al., 2017; Clift et al., 2014;
411 Dosseto et al., 2015). As shown in Fig. 4a for the last 110 kyrs, in core MS27PT, the Nd
412 isotopic compositions of clay-size fractions are systematically more radiogenic (and vary less)
413 than ϵNd values of the corresponding silt-size fractions. This suggests a dominant basaltic
414 source for the clays, which are mostly issued from the Ethiopian Traps region, in contrast to
415 the silts that may derive from different provenance regions.

416 For the last 16 kyrs, a “source-to-sink” approach could be developed by comparing the clay
417 signals extracted from both the NDSF and the Lake Tana sediment records; this latter being
418 located ~3500 km upstream, in the Ethiopian Highlands. During this period, clay ϵNd values
419 for sediment deposited in the Lake Tana remained constantly high, with a mean value of $2 \pm$
420 0.25 (Fig. 3a; in agreement with the regional lithology), similar – within uncertainties - to the
421 ϵNd value of 1.8 ± 0.8 measured in mud sediments carried at present by the Blue Nile River
422 (Garzanti et al., 2015; Fig. 3a). Most likely, the clays transported by the Blue Nile, Atbara and
423 Sobat rivers were formed locally within the soils developed above basaltic and rhyolitic
424 Ethiopian Traps sequences. Differently from Blue Nile/Atbara rivers, the Ethiopian Traps
425 radiogenic signature of the Sobat River would be originated from the Lake Turkana overflow
426 events (towards the lower White Nile basin) occurring during humid periods (Johnson and
427 Malala, 2009).

428 During the last 16 kyrs, clay $\delta^7\text{Li}$ values are similar in the MS27PT core and in the Lake Tana
429 core (Fig. 3b). This first confirms that most of the clay material exported to the NDSF at this
430 period came from the Ethiopian Highlands, and that measured $\delta^7\text{Li}$ compositions can actually
431 reflect weathering conditions, without being significantly affected by sediment transport nor
432 by any post-depositional effect related to diagenetic processes.

433 In contrast, clays from MS27PT sediment exhibit lower ϵNd values (mean value of -4.36 ,
434 $n=94$) than for the Lake Tana (mean value of 2 , $n=13$ for the last 14 kyr; Fig. 3a and 4a) over
435 the last 110.000 years. However, Blue Nile sources remains relatively stable and high
436 compared to the Bahr el Jebel/White Nile sources (Fig. 4a). In fact, a small increase in the
437 contribution of clay-size material from the Central African Craton ($\epsilon\text{Nd} \sim -30$) has a
438 significant impact on ϵNd values. This effect likely explains the bias observed between clay
439 ϵNd values from core MS27PT and from Lake Tana sediments.

440 The smectite abundance measured in the clay fractions over the last 110 kyrs also remains
441 high (> 65%), suggesting that ϵNd signature and smectite clay contribution are both sensitive
442 to clay sources (Figs. 2 and 4). Thus, our “source-to-sink” approach demonstrates that clays
443 from the Ethiopian Traps (Blue Nile/Atbara and Sobat rivers) represent the dominant
444 sediment source to the NDSF sediment for the last 110 kyrs (Fig. 4). In contrast, clays derived
445 from Saharan dust (Saharan Metacraton) and from the Bahr el Jebel/White Nile (Cetral
446 African Craton) or from the Red Sea Hills (Arabian Nubian Shield) contribute comparatively
447 in much lower proportion. Importantly, ϵNd show that the proportion of Ethiopian Traps-
448 originated clays remains high (ϵNd values oscillate between -8 and -2) even during arid
449 periods, suggesting persistent soil and clay formation over the Ethiopian Highlands.

450

451 **5.1.2. Threshold effects on sediment transport during the Younger Dryas**

452 During arid periods the increased difference in ϵNd values between clays and silts from the
453 NSDF (Fig. 4a) suggest that both particle types come from different and lithologically
454 contrasted regions. Thus, the variable ϵNd difference between clays and silts could be
455 explained by different size-dependent transport processes, as well as by possible threshold
456 effects on the transport of coarser particles. This aspect is well illustrated when considering
457 the Younger Dryas period (YD; Fig. 5). In northern Africa, the Younger Dryas is generally
458 associated with a relatively arid period from ~13 and ~12 kyr BP, resulting from a weakening
459 of monsoon intensity (Garcin et al., 2007) and from the fall of lakes level (Roberts et al.,
460 1993; Stager and Johnson, 2008). In core MS27PT, this period is highlighted by
461 progressively decreasing sediment Ti/Ca ratios, consistent with lower terrigenous inputs (Fig.
462 5, Revel et al., 2015, 2014, 2010). At the same time, the clay ϵNd composition remained near
463 constant and high (-2). In contrast, silt ϵNd display an abrupt trend towards lower (less
464 radiogenic) isotopic signatures, by about 3 epsilon units. This shift, associated with the

465 decrease of Ti/Ca ratio, can hence only be explained by a major reduction in the export of
466 coarse-grained particles from the Ethiopian Traps source region, together with presumably
467 more important sediment contributions from the Sahara dust, or from the Bahr el Jebel/White
468 Nile. Accordingly, during humid periods, the Nile flood-induced silty deposits are similar
469 (higher ϵNd values) than clay fraction, showing a strong hydro-systems' reactivation in
470 Ethiopian Highlands in link to high insolation patterns (Mologni et al., 2020).

471 Overall, during the YD, the observed size-dependent trends observed for Nd isotopes and
472 mineralogical investigations appear in agreement with a possible reduced rainfall resulting in
473 weaker river transport energy of the silts derived for the Ethiopian Traps. Contrarily, the
474 origin and the transport of suspended clays from the Ethiopian Highlands appeared to have
475 remained globally unchanged. This may suggest that the onset of arid conditions in the
476 Ethiopian Highlands led to reduced transport of coarse particles by the Blue Nile river in link
477 with reduced hydrological activity.

478 Lower ϵNd values of the silt fraction during arid periods may be the result of combined
479 climatic and geomorphic processes occurring along the Nile River headwaters. Higher
480 precipitations over the 'Equatorial' Nile (Bahr el Jebel/White Nile; 4°S - 3°N; Fig. 1)
481 supported by the ITCZ southward migration, with respect to northern Blue Nile sources (9-
482 15°N), would be the hydro-climatic driver of this process. However, Williams (2019)
483 indicated that during White Nile low flow periods, the Sudd swamps dried out, taking a few
484 centuries to re-establish during the subsequent humid phase. Thus, the absence of the filtering
485 swamps effect could have permitted an enhanced coarse particle discharge, making the Bahr
486 el Jebel/White Nile hydro-sedimentary system excessively reactive to precipitations during or
487 immediately after arid periods. Finally, low silt ϵNd during arid periods can be even
488 attributable to an aeolian coarser source derived from the Saharan Metacraton or from the Red
489 Sea Hills erosion (Macgregor, 2012; Palchan et al., 2013).

490 Our results show that the combination of Nd isotopic compositions in both clay and silt size
491 fractions constitutes a powerful tool for evidencing differential transport processes
492 mechanisms in response to the YD climatic forcing.

493

494 **5.1.3. Threshold effects on transport related to insolation minima and maxima**

495 The low insolation period ranged between 50 and 40 kyrs BP is characterized in MS27PT
496 core by a slight decrease only of both clay Ti/Ca ratio and ϵNd (Fig. 6e, f and g). The lack of
497 significant geochemical changes during this specific arid period could be explained by a
498 threshold effect of insolation on sediment transport efficiency. Indeed, the decrease in
499 insolation around 445 W/m^2 (and corresponding monsoon activity) was not as strong as
500 during other arid periods when the 15°N insolation value was much weaker in magnitude ($<$
501 440 W/m^2 ; Fig. 6e). From an astronomic point of view, at 45 kyr BP, the eccentricity was low
502 and modulated the precession, with consequently a small decrease of the insolation value (Fig.
503 6a, b and c). This particular orbital configuration and the resulting small decrease in local
504 insolation could be responsible for a limited increase of the Nile flood activity.

505 A similar threshold effect might have occurred during periods of maxima insolation, which
506 are usually expected to be related to humid climate and development of Sapropel layers in the
507 Eastern Mediterranean Sea (Emeis et al., 2003; Rohling et al., 2015; Rossignol-Strick et al.,
508 1982). Five high insolation periods occurred during the last 110 kyr (Fig. 6e). However, only
509 3 sapropel layers (S1, S3, S4) were recorded in the MS27PT sediment, as inferred from their
510 high sulphur contents (Fig. 6d) suggesting a non-linear response of sapropel events to
511 insolation patterns. The absence of sulfur along with a slight increase in Ti/Ca ratio during the
512 high insolation period centered around 55 kyr and around 33 kyr suggest that particulate and
513 freshwater river discharges did not increase significantly at that time, in contrast to S1, S3 and

514 S4. Similarly, a threshold effect during insolation maxima periods was evidenced in the
515 Sanbao-Hulu speleothem (Wang et al., 2008), indicating possible decoupling between
516 insolation and monsoon activity (Ziegler et al., 2010).

517 From a continental point of view of the Nile river functioning, the installation of the Gezira
518 mega-fan (in the lower Blue and White valleys) at 41 ka and also at around 55 ka, with an
519 overbank flooding suggesting wetter condition upstream in the Blue Nile headwaters
520 (Williams et al., 2015). Geomorphological study evidences the presence of the Dinder, a
521 seasonal tributary attesting increase in terrigenous and freshwater inputs in the lower Blue
522 Nile region (Williams, 2019; Williams et al., 2015). However, the deltaic sediments do not
523 record an enhanced sediment transport at that time. Also, at 33 kyrs BP the obliquity was low
524 (inclination of the earth's axe of rotation is of 22.5° : Fig. 6b) and could modulate the
525 precession, with consequently a smaller increase of the insolation value compared to the AHP.
526 Thus, this particular orbital configuration could be responsible for a limited increase in
527 monsoon intensity and associated Nile flood activity, explaining the more negative ϵNd value
528 of -4 compared to the AHP.

529 It is not excluded that geomorphological changes along the White Nile branch may explain
530 the subtle ϵNd variations observed among humid periods. For example, towards 27 kyrs, there
531 is good evidence of very high White Nile flow synchronous with a phase of alluvial fan
532 activity near Jebelein (Williams et al., 2010). As indicated by Williams (2019), during humid
533 periods the exceptionally high Blue Nile flow caused a dam effect on White Nile
534 water/sediment inputs, creating a vast seasonal lake in which fine mud accumulated. During
535 arid periods, reduced Blue Nile flow allows the White Nile mega-lake regression and the
536 erosion and transport of low radiogenic (ϵNd) sediments contained within it. Similar to Sudd
537 swamps functioning during YD (see Section 5.1.2), the White Nile solid discharge would
538 have been subjected to hydro-geomorphic processes partially decoupled from climatic

539 forcing, which could explain variations in more negative ϵNd values recorded in the NDSF
540 sediments during arid periods.

541

542 **5.2. Relationships between climate and continental weathering**

543 **5.2.1 Sources vs weathering**

544 Measured variations of weathering proxies such as mobile/immobile element ratios (e.g.
545 Mg/Ti and K/Ti) and $\delta^7\text{Li}$ in clays can be equally affected by changes in weathering
546 conditions and by sediment provenance. In core MS27PT, the increase of clay K/Ti ratios
547 during arid periods (see yellow bands in Fig. 2) could possibly be explained by enhanced
548 contribution of K-rich illite from presumably source regions characterized by relatively low
549 ϵNd values (Saharan dust and/or Bahr el Jebel/White Nile River particles), despite the fact
550 that there is no clear relationships between illite contents and insolation (Figs. 2 and 4, Table
551 S2). Alternatively, downcore K/Ti variations could result from changes in the leaching
552 degree, since potassium is an alkali element mostly mobile during chemical weathering (Fig.
553 2e). As already discussed in Bastian et al., (2017), evidence that the clay K/Ti trend in core
554 MS27PT evolves similarly with Mg/Ti first supports that they both are controlled by
555 weathering. This is because K and Mg in clay-size fractions are preferentially hosted by
556 distinct secondary mineral phases, e.g illite vs smectite, respectively. It should be noted that
557 the amplitude of the variations in K/Ti and Mg/Ti ratios during the MIS4 arid period is similar
558 to HS4 and HS5 Heinrich events, whereas the amplitude of the Nd variations remain small for
559 HS4 and HS5 (Fig. 2). This suggests that clay K/Ti and Mg/Ti ratios may be controlled by the
560 two processes (change in source and in weathering), but at a different degree, depending on
561 the climate event intensity or location.

562 Concerning the control of Li isotopes, the ϵNd vs $\delta^7\text{Li}$ diagram (Fig. 7) shows that there is no
563 simple correlation between these proxies. Clay samples with similar $\delta^7\text{Li}$ values ($\sim 2\text{‰} \pm 0.5\text{‰}$)
564 can display a wide range of ϵNd values (Fig. 7a), and vice versa. Also, there is no visible
565 relationship between $\delta^7\text{Li}$ and clay Li/Al, in contrast with river SPM, which are mostly
566 controlled by mineral mixing (Dellinger et al., 2017) (see SI). As a consequence, variations in
567 clay $\delta^7\text{Li}$ compositions during the last 110 kyrs most likely reflect weathering variations, in
568 agreement with previous studies (e.g. Pogge von Strandmann et al., 2017, 2010, 2020;
569 Dellinger et al., 2017, 2015, 2014; Bastian et al., 2017; Vigier et al., 2009). This is
570 particularly evident for several specific arid periods (H2, H4, LGM) during which clay $\delta^7\text{Li}$
571 exhibit a large range of values but without any particular change in ϵNd (Figs. 7b and 9).
572 These arid periods are also characterized by the highest $\delta^7\text{Li}$ values measured in clays. As
573 described in the Introduction, these high $\delta^7\text{Li}$ values reflect a more incongruent weathering
574 and a lower (leaching / neoformation) ratios, and are consistent with lower leaching rates
575 under less intensive monsoonal precipitation. In contrast, no clear systematics can be
576 highlighted for humid periods characterized by high and homogeneous ϵNd values, since the
577 AHP clays display significantly lower $\delta^7\text{Li}$ values compared to the 80 and 105 kyr humid
578 periods (MIS 5a and 5c; Figs. 6 and 9).

579

580 **5.2.2 Impact of monsoon intensity oscillation and of temperature variations**

581 For the AHP (~ 14.5 - ~ 6 kyrs), the MIS 5a (~ 86 - ~ 75 kyrs) and the MIS 5c (~ 96 kyrs) humid
582 periods, elevated insolation maxima indicate higher monsoonal precipitation and freshwater
583 discharge across the Nile River Basin, as traced by more radiogenic Nd signature, during
584 sapropels S1, S3 and S4 (Fig. 6). Thus, one would expect that these three humid periods were
585 associated with low clay $\delta^7\text{Li}$ values, as observed during the AHP and explained by higher
586 leaching rate (Bastian et al., 2017). However, during MIS5a and 5c, clay $\delta^7\text{Li}$ are significantly

587 higher (~3.5‰) than during the AHP (~1.7‰). This feature may be related with the observed
588 differences in the magnitude of insolation maxima: 470W/m² during the AHP vs 480 W/m²
589 during MIS5a and 5c, leading to distinct variations of the precipitation pattern (Fig. 6e).

590 An alternative explanation would be that soil and vegetation covers prior to the onset of
591 increasing monsoon were different for each of these periods, resulting in a different
592 weathering response. Since the Eemien period and before the onset of S4 and S3,
593 environmental conditions were warmer and probably more humid than during the Last Glacial
594 Period (~75 – ~25 kyrs BP; Kutzbach et al., 2020; Lisiecki and Raymo, 2005). Indeed, in
595 North and West Africa, the Last Interglacial period (until MIS 5d; ~130 – ~110 kyrs BP) was
596 characterized by enhanced humidity and by the expansion of rain forest (Dupont et al., 2000)
597 composed by common C₃ plants, suggesting the spread of trees and soil development in the
598 sub-Saharan area (Castañeda et al., 2009a; Williams, 2019). After ~110 kyrs BP, the response
599 of weathering to precipitation changes between MIS 5c and 5a periods could have been higher
600 than during the AHP, which followed the LGM period characterized by reduced soil thickness
601 and vegetation cover. Additional work would be needed to further explore these aspects.

602 Another interesting feature displayed by Li isotopes downcore MS27PT is the progressive
603 decrease of the clay $\delta^7\text{Li}$ baseline values between 110 kyr and 25 kyr, which appears to mimic
604 the planktonic foraminiferal $\delta^{18}\text{O}$ signal (Figs. 8a, 8c and S1). This covariation suggests an
605 influence of regional temperature on the weathering incongruency ratio at the scale of the Nile
606 Basin. Over the last 110 kyr, estimates for air temperatures in tropical Africa display
607 variations in relation with glacial-interglacial climatic variability. These estimations are based
608 on various proxy records from lake (Tierney et al., 2008) and marine (Hijmans et al., 2005;
609 Molliex et al., 2019) sediments, and from Soreq cave speleothem reconstructions (Affek et al.,
610 2008; Mcgarry et al., 2004; Pogge von Strandmann et al., 2017; Fig. 8b). Also, temperature in
611 the last glacial tropical Africa was estimated to be about 3-5°C cooler than today (LGM,

612 Kelly et al., 2014; Schefuß et al., 2005). Based on the above, we speculate that a progressive
613 cooling in North-East Africa between ~110 and ~25 kyrs could possibly explain the
614 progressive decrease of the $\delta^7\text{Li}$ minima values, in response to gradual changes in soil
615 conditions within the Nile Basin. This would be in agreement with a recent investigation of
616 speleothems from the Soreq cave in Israel (Fig. 8b; Pogge von Strandmann et al., 2017),
617 which suggested a weakening of continental weathering over glacial/interglacial cycles due to
618 decreasing temperatures. Thus, in contrast to rainfall changes, which presumably result in
619 rapid response of leaching rates, gradual temperature evolution can affect soil conditions and
620 clay neoformation rates over the long-term only (>10kyr). Li isotopes in clay-size fractions
621 from the NSDF therefore suggest a decoupled response of continental weathering to
622 temperature and precipitation changes.

623

624 **5.2.3 Synchronous timing with Heinrich stadials**

625 During the last glacial period (~75 – ~25 kyrs BP), the evolution of global climate was
626 punctuated by abrupt instabilities, recorded in the Greenland ice $\delta^{18}\text{O}$ signals as Dansgaard-
627 Oeschger cycles (DO; Bond et al., 1993; Dansgaard et al., 1993). These cycles were
628 characterized by the succession of rapid shifts towards higher (interstadial) and lower (stadial)
629 temperature in the northern latitudes (Sanchez Goñi and Harrison, 2010), presumably
630 resulting from changing ocean circulation patterns (e.g. Waelbroeck et al., 2018). Some DO
631 stadials were associated with episodes of massive iceberg discharge in the North Atlantic
632 (referred to as Heinrich Stadial [HS], Heinrich, 1988; Hemming, 2004). The HS events and
633 other northern hemisphere cold episodes, such as the YD, were associated to arid conditions
634 in northern Africa (Shanahan et al., 2015; Verschuren et al., 2009). The mechanism
635 responsible for this aridification is still under debate. One explanation is that Atlantic
636 Meridional Oceanic Circulation (AMOC) reduction at that time led to the southward

637 migration of the ITCZ and monsoon rain belt, leading to regional aridification in North
638 Africa, as testified by increase in the delivery of Saharan dust along the western African
639 ocean margins (Collins et al., 2013; Heinrich et al., 2021; Le Quilleuc et al., submitted) or by
640 δD_{wax} displayed by lake sediment records (Tierney et al., 2008). Instead, a recent study
641 (Collins et al., 2017) suggests that reorganisation of the tropical jet stream and atmospheric
642 circulation patterns may have played an important role in the monsoon variability at that time.
643 This could explain the sudden shifts towards aridification in northern Africa during HS
644 events. In any case, the fact is that North Atlantic cooling episodes are recorded in
645 sedimentary archives from tropical regions in Africa. For instance, δD_{wax} records in Lake
646 Tanganyika and Lake Challa (Tierney et al., 2008) indicate reduced precipitation during HS1
647 (≈ 16 kyrs) to HS5 (≈ 47 kyrs). Desiccation of Lake Tana during HS1 coincides with drying of
648 Lake Victoria, source of the White Nile water, underlining the sensitivity of the entire Nile
649 basin to climatic extremes (Lamb et al., 2018; Stager and Johnson, 2008; Talbot and Lærdal,
650 2000).

651 In NDSF core MS27PT, weathering proxy records (Mg/Ti, K/Ti and $\delta^7\text{Li}$) are clearly in phase
652 with the North Atlantic climate instabilities (see Fig. 9). The observed shift towards heavier
653 (higher) clay $\delta^7\text{Li}$ values during arid periods is consistent with reduced leaching under more
654 arid conditions. The variation amplitude of weathering proxies is quite large during HS1,
655 HS2, HS4 and HS5 events, and comparatively smaller during HS3. This observation is
656 comparable to aeolian dust records from the western African margin (Collins et al., 2013;
657 Heinrich et al., 2021). For some of these events (e.g. HS4) clay ϵ_{Nd} vary little, suggesting a
658 lack of control from clay provenance, as detailed in section 5.2.1, but this would need to be
659 refined at a higher temporal resolution. Overall, these observations reinforce the idea that past
660 $\delta^7\text{Li}$ variations have been primarily driven by monsoon intensity and suggest that abrupt

661 climate changes - originally initiated in the northern hemisphere high-latitudes - may have
662 influenced weathering processes in northern Africa.

663 Our results suggest a temporal synchronization between North Atlantic climate variations,
664 monsoon variability and silicate weathering in northern Africa. Evidence for a timely
665 response of chemical weathering to tropical monsoon has important implications for
666 predicting the possible future impact of global warming in tropical regions. A recent modeling
667 study (Defrance et al., 2017) predicts a future reduction of rainfall in northern Africa (Sahel,
668 Ethiopia) due to temperature anomalies and changes in wind direction. Since these areas are
669 densely populated and heavily dependent on rainfall and water availability, a rapid change in
670 soil resources may have strong consequences for local populations.

671

672 **6. Conclusions**

673 We applied various geochemical proxies ($\delta^7\text{Li}$, ϵNd and elementary ratios) to clay-size
674 sediment fractions from both marine (core MS27PT) and lacustrine (Lake Tana) sediments in
675 order to better understand the impact of African monsoon fluctuations on erosion and
676 chemical weathering processes within the Nile Basin during the Late Quaternary.

677 Based on Nd isotopes, we showed that the Ethiopian Traps area represented the main
678 contributor of clays to the NDSF for the last 110,000 years. The use of Li isotopes as
679 weathering proxies in this basin was evaluated by comparing Li isotope measurements from
680 core MS27PT and Lake Tana sediment records, indicating no significant change of the clay
681 $\delta^7\text{Li}$ values during the ~3000 km transport by the Nile River.

682 We find that fluctuations of clay-size particle contributions to the Nile Delta are mainly
683 driven by orbital precession cycle, which controls the African monsoon intensity variations.
684 Nevertheless our results indicate a non-linear response of the Nile sources and chemical

685 weathering to the insolation forcing. Finally, a decoupling between temperature and
686 precipitation is found concerning their respective impact on chemical weathering. A decrease
687 of mineral leaching rates in soils is inferred from Li isotopes during several Heinrich Stadials,
688 with no significant time lag relative to North Atlantic climatic events. This synchronous
689 timing evidences a rapid response of continental weathering to hydroclimate changes.

690

691 **Acknowledgments**

692 This work was financially supported by BQR Geoazur and OCA, INSU-SYSTER grants and
693 the ANR INTOCC (ANR-15-CE31-0013). The MS27PT core was recovered during the
694 MIMES cruise. We thank A. De Prunelé and Y. Germain for assistance during MC-ICPMS
695 analyses at IFREMER. O. Bruguier from the Montpellier university is acknowledged for
696 assistance during MC-ICPMS analyses realized at the AETE-ISO platform.

697

698 **Author contributions**

699 Marie Revel and Nathalie Vigier led the project and helped with interpretation and writing.
700 Luc Bastian performed sediment sampling, treatment and all Li isotope analyses. Marie-
701 Emmanuelle Kerros helped with the sediment pre-treatment and clay extractions. Luc Bastian
702 and Carlo Mologni led the writing. Germain Bayon performed Nd isotope analyses on Nile
703 delta clays and helped with interpretation. Delphine Bosch was in charge with Nd isotope
704 analyses of Tana Lake sediments. Christophe Colin performed clay mineralogy in Nile Delta
705 sediments and helped with interpretation. Henry Lamb provided us the lake Tana samples
706 already dated. All authors contributed to data interpretation and writing finalization.

707

708 **Additional Information**

709 Luc Bastian and Carlo Mogni, on behalf of all authors of the paper, declare that there are no
710 competing financial interests in relation to the work described.

711

References

712

- 713 Abdelsalam, M.G., Liégeois, J.-P., Stern, R.J., 2002. The Saharan Metacraton. *Journal of African Earth*
714 *Sciences* 34, 119–136. [https://doi.org/10.1016/S0899-5362\(02\)00013-1](https://doi.org/10.1016/S0899-5362(02)00013-1)
- 715 Affek, H.P., Bar-matthews, M., Ayalon, A., Matthews, A., Eiler, J.M., 2008. Glacial / interglacial
716 temperature variations in Soreq cave speleothems as recorded by ‘ clumped isotope ’
717 thermometry. *Geochimica et Cosmochimica Acta* 72, 5351–5360.
718 <https://doi.org/10.1016/j.gca.2008.06.031>
- 719 Almogi-Labin, A., Bar-Matthews, M., Shriki, D., Kolosovsky, E., Paterne, M., Schilman, B., Ayalon, A.,
720 Aizenshtat, Z., Matthews, A., 2009. Climatic variability during the last ~90 ka of the southern
721 and northern Levantine Basin as evident from marine records and speleothems. *Quaternary*
722 *Science Reviews* 28, 2882–2896. <https://doi.org/10.1016/j.quascirev.2009.07.017>
- 723 Andersen, K.K., Azuma, N., and North Greenland Ice Core Project members, 2004. High-resolution
724 record of Northern Hemisphere climate extending into the last interglacial period. *Nature*.
725 <https://doi.org/10.1038/nature02805>
- 726 Bahr, A., Kaboth, S., Jiménez-Espejo, F.J., Sierro, F.J., Voelker, A.H.L., Lourens, L., Röhl, U., Reichert,
727 G.J., Escutia, C., Hernández-Molina, F.J., Pross, J., Friedrich, O., 2015. Persistent monsoonal
728 forcing of mediterranean outflow water dynamics during the late Pleistocene. *Geology* 43,
729 951–954. <https://doi.org/10.1130/G37013.1>
- 730 Balter, V., Vigier, N., 2014. Natural variations of lithium isotopes in a mammalian model. *Metallomics*
731 6, 582–586. <https://doi.org/10.1039/c3mt00295k>
- 732 Bastian, L., Revel, M., Bayon, G., Dufour, A., Vigier, N., 2017. Abrupt response of chemical weathering
733 to Late Quaternary hydroclimate changes in northeast Africa. *Scientific Reports* 7, 44231.
734 <https://doi.org/10.1038/srep44231>
- 735 Bastian, L., Vigier, N., Revel, M., Bayon, G., 2018. Lithium Isotope Composition of Marine Biogenic
736 Carbonates and Related Reference Materials 42, 403–415.
737 <https://doi.org/10.1111/ggr.12218>
- 738 Bastian, L., Vigier, N., Revel, M., Yirgu, G., Ayalew, D., Pik, R., 2019. Chemical erosion rates in the
739 upper Blue Nile Basin and related atmospheric CO₂ consumption. *Chemical Geology* 518, 19–
740 31. <https://doi.org/10.1016/j.chemgeo.2019.03.033>
- 741 Bayon, G., Dennielou, B., Etoubleau, J., Ponzevera, E., Toucanne, S., Bermell, S., 2012. Intensifying
742 weathering and land use in iron age Central Africa. *Science* 335, 1219–1222.
743 <https://doi.org/10.1126/science.1215400>
- 744 Bayon, G., Toucanne, S., Skonieczny, C., André, L., Bermell, S., Cheron, S., Dennielou, B., Etoubleau, J.,
745 Freslon, N., Gauchery, T., Germain, Y., Jorry, S.J., Ménot, G., Monin, L., Ponzevera, E., Rouget,
746 M.L., Tachikawa, K., Barrat, J.A., 2015. Rare earth elements and neodymium isotopes in
747 world river sediments revisited. *Geochimica et Cosmochimica Acta* 170, 17–38.
748 <https://doi.org/10.1016/j.gca.2015.08.001>
- 749 Beaulieu, E., Goddèris, Y., Donnadiou, Y., Labat, D., Roelandt, C., 2012. High sensitivity of the
750 continental-weathering carbon dioxide sink to future climate change. *Nature Climate Change*
751 2, 346–349. <https://doi.org/10.1038/nclimate1419>
- 752 Berger, A., Loutre, M.F., 1991. Insolation values for the climate of the last 10 million years.
753 *Quaternary Science Reviews* 10, 297–317. [https://doi.org/10.1016/0277-3791\(91\)90033-Q](https://doi.org/10.1016/0277-3791(91)90033-Q)
- 754 Berke, M.A., Johnson, T.C., Werne, J.P., Grice, K., Schouten, S., Sinninghe Damsté, J.S., 2012.
755 Molecular records of climate variability and vegetation response since the Late Pleistocene in
756 the Lake Victoria basin, East Africa. *Quaternary Science Reviews* 55, 59–74.
757 <https://doi.org/10.1016/j.quascirev.2012.08.014>

758 Blanchet, C.L., Contoux, C., Leduc, G., 2015. Runoff and precipitation dynamics in the Blue and White
759 Nile catchments during the mid-Holocene: A data-model comparison. *Quaternary Science*
760 *Reviews* 130, 222–230. <https://doi.org/10.1016/j.quascirev.2015.07.014>
761 Blanchet, C.L., Frank, M., Schouten, S., 2014. Asynchronous changes in vegetation, runoff and Erosion
762 in the Nile River watershed during the Holocene. *PLoS ONE* 9, 1–18.
763 <https://doi.org/10.1371/journal.pone.0115958>
764 Blanchet, C.L., Osborne, A.H., Tjallingii, R., Ehrmann, W., Friedrich, T., Timmermann, A., Brückmann,
765 W., Frank, M., 2021. Drivers of river reactivation in North Africa during the last glacial cycle.
766 *Nature Geoscience* 1–7. <https://doi.org/10.1038/s41561-020-00671-3>
767 Blanchet, C.L., Tjallingii, R., Frank, M., Lorenzen, J., Reitz, A., Brown, K., Feseker, T., Brückmann, W.,
768 2013. High- and low-latitude forcing of the Nile River regime during the Holocene inferred
769 from laminated sediments of the Nile deep-sea fan. *Earth and Planetary Science Letters* 364,
770 98–110. <https://doi.org/10.1016/j.epsl.2013.01.009>
771 Blanchet, C.L., Tjallingii, R., Schleicher, A.M., Schouten, S., Frank, M., Brauer, A., 2020. Deoxygenation
772 dynamics above the western Nile deep-sea fan during sapropel S1 at seasonal to millennial
773 time-scales (preprint). *Teleconnections/Marine Archives/Holocene*.
774 <https://doi.org/10.5194/cp-2020-114>
775 Bond, G., Broecker, W., Johnsen, S., McManus, J., Labeyrie, L., Jouzel, J., Bonani, G., 1993.
776 Correlations between climate record from North Atlantic sediments and Greenland ice.
777 *Nature* 365, 143–147.
778 Bouchez, J., Blanckenburg, F. von, Schuessler, J.A., 2013. Modeling novel stable isotope ratios in the
779 weathering zone. *American Journal of Science* 313, 267–308.
780 <https://doi.org/10.2475/04.2013.01>
781 Bouimetarhan, I., Prange, M., Schefuß, E., Dupont, L., Lippold, J., Mulitza, S., Zonneveld, K., 2012.
782 Sahel megadrought during Heinrich Stadial 1: Evidence for a three-phase evolution of the
783 low- and mid-level West African wind system. *Quaternary Science Reviews* 58, 66–76.
784 <https://doi.org/10.1016/j.quascirev.2012.10.015>
785 Bouvier, A., Vervoort, J.D., Patchett, P.J., 2008. The Lu-Hf and Sm-Nd isotopic composition of CHUR:
786 Constraints from unequilibrated chondrites and implications for the bulk composition of
787 terrestrial planets. *Earth and Planetary Science Letters* 273, 48–57.
788 <https://doi.org/10.1016/j.epsl.2008.06.010>
789 Carignan, J., Vigier, N., Millot, R., 2007. Three secondary reference materials for lithium isotope
790 measurements: Li7-N, Li6-N and LiCl-N solutions. *Geostandards and Geoanalytical Research*
791 31, 7–12. <https://doi.org/10.1111/j.1751-908X.2007.00833.x>
792 Castañeda, I.S., Mulitza, S., Schefuß, E., Santos, R.A.L. dos, Damsté, J.S.S., Schouten, S., 2009a. Wet
793 phases in the Sahara/Sahel region and human migration patterns in North Africa. *PNAS* 106,
794 20159–20163. <https://doi.org/10.1073/pnas.0905771106>
795 Castañeda, I.S., Schouten, S., Pätzold, J., Lucassen, F., Kasemann, S., Kuhlmann, H., Schefuß, E., 2016.
796 Hydroclimate variability in the Nile River Basin during the past 28,000 years. *Earth and*
797 *Planetary Science Letters* 438, 47–56. <https://doi.org/10.1016/j.epsl.2015.12.014>
798 Castañeda, I.S., Werne, J.P., Johnson, T.C., Filley, T.R., 2009b. Late Quaternary vegetation history of
799 southeast Africa: The molecular isotopic record from Lake Malawi. *Palaeogeography,*
800 *Palaeoclimatology, Palaeoecology* 275, 100–112.
801 <https://doi.org/10.1016/j.palaeo.2009.02.008>
802 Caves Rugenstein, J.K., Ibarra, D.E., von Blanckenburg, F., 2019. Neogene cooling driven by land
803 surface reactivity rather than increased weathering fluxes. *Nature* 571, 99–102.
804 <https://doi.org/10.1038/s41586-019-1332-y>
805 Chauvel, C., Blichert-toft, J., 2001. A hafnium isotope and trace element perspective on melting of
806 the depleted mantle. *Earth and Planetary Science Letters* 190.
807 Chen, Q., Liu, Z., Kissel, C., 2017. Clay mineralogical and geochemical proxies of the East Asian
808 summer monsoon evolution in the South China Sea during Late Quaternary. *Scientific*
809 *Reports* 7, 42083. <https://doi.org/10.1038/srep42083>

810 Clift, P.D., Kulhanek, D.K., Zhou, P., Bowen, M.G., Vincent, S.M., Lyle, M., Hahn, A., 2020. Chemical
811 weathering and erosion responses to changing monsoon climate in the Late Miocene of
812 Southwest Asia. *Geol. Mag.* 157, 939–955. <https://doi.org/10.1017/S0016756819000608>
813 Clift, P.D., Wan, S., Blusztajn, J., 2014. Reconstructing chemical weathering, physical erosion and
814 monsoon intensity since 25Ma in the northern South China Sea: A review of competing
815 proxies. *Earth-Science Reviews* 130, 86–102. <https://doi.org/10.1016/j.earscirev.2014.01.002>
816 Collins, J.A., Govin, A., Mulitza, S., Heslop, D., Zabel, M., Hartmann, J., Röhl, U., Wefer, G., 2013.
817 Abrupt shifts of the Sahara-Sahel boundary during Heinrich stadials. *Climate of the Past* 9,
818 1181–1191. <https://doi.org/10.5194/cp-9-1181-2013>
819 Collins, J.A., Prange, M., Caley, T., Gimeno, L., Beckmann, B., Mulitza, S., Skonieczny, C., Roche, D.,
820 Schefuß, E., 2017. Rapid termination of the African Humid Period triggered by northern high-
821 latitude cooling. *Nature Communications* 8. <https://doi.org/10.1038/s41467-017-01454-y>
822 Collins, J.A., Schefuß, E., Heslop, D., Mulitza, S., Prange, M., Zabel, M., Tjallingii, R., Dokken, T.M.,
823 Huang, E., MacKensen, A., Schulz, M., Tian, J., Zarriess, M., Wefer, G., 2011. Interhemispheric
824 symmetry of the tropical African rainbelt over the past 23,000 years. *Nature Geoscience* 4,
825 42–45. <https://doi.org/10.1038/ngeo1039>
826 Cornuault, M., Vidal, L., Tachikawa, K., Licari, L., Rouaud, G., Sonzogni, C., Revel, M., 2016. Deep
827 water circulation within the eastern Mediterranean Sea over the last 95kyr: New insights
828 from stable isotopes and benthic foraminiferal assemblages. *Palaeogeography,*
829 *Palaeoclimatology, Palaeoecology* 459, 1–14. <https://doi.org/10.1016/j.palaeo.2016.06.038>
830 Costa, K., Russell, J., Konecky, B., Lamb, H., 2014. Isotopic reconstruction of the African Humid Period
831 and Congo Air Boundary migration at Lake Tana, Ethiopia. *Quaternary Science Reviews* 83,
832 58–67. <https://doi.org/10.1016/j.quascirev.2013.10.031>
833 Dansgaard, W., Johnsen, S.J., Clausen, H.B., Dahl-Jensen, D., Gundestrup, N.S., Hammer, C.U.,
834 Hvidberg, C.S., Steffensen, J.P., Sveinbjörnsdóttir, A.E., Jouzel, J., Bond, G., 1993. Evidence for
835 general instability of past climate from a 250-kyr ice-core record. *Nature* 364, 218–220.
836 De Lange, G.J., Thomson, J., Reitz, A., Slomp, C.P., Speranza Principato, M., Erba, E., Corselli, C., 2008.
837 Synchronous basin-wide formation and redox-controlled preservation of a Mediterranean
838 sapropel. *Nature Geoscience* 1, 606–610. <https://doi.org/10.1038/ngeo283>
839 Defrance, D., Ramstein, G., Charbit, S., Vrac, M., Famién, A.M., Sultan, B., Swingedouw, D., Dumas, C.,
840 Gemenne, F., Alvarez-Solas, J., Vanderlinden, J.-P., 2017. Consequences of rapid ice sheet
841 melting on the Sahelian population vulnerability. *Proceedings of the National Academy of*
842 *Sciences* 114, 6533–6538. <https://doi.org/10.1073/pnas.1619358114>
843 Dellinger, M., Bouchez, J., Gaillardet, J., Faure, L., Moureau, J., 2017. Tracing weathering regimes
844 using the lithium isotope composition of detrital sediments. *Geology* 45, 411–414.
845 <https://doi.org/10.1130/G38671.1>
846 Dellinger, M., Gaillardet, J., Bouchez, J., Calmels, D., Louvat, P., Dosseto, A., Gorge, C., Alanoca, L.,
847 Maurice, L., 2015. Riverine Li isotope fractionation in the Amazon River basin controlled by
848 the weathering regimes. *Geochimica et Cosmochimica Acta* 164, 71–93.
849 <https://doi.org/10.1016/j.gca.2015.04.042>
850 Dellinger, M., Gaillardet, J., Bouchez, J., Calmels, D., Galy, V., Hilton, R.G., Louvat, P., France-
851 Lanord, C., 2014. Lithium isotopes in large rivers reveal the cannibalistic nature of modern
852 continental weathering and erosion. *Earth and Planetary Science Letters* 401, 359–372.
853 <https://doi.org/10.1016/j.epsl.2014.05.061>
854 Demenocal, P., Ortiz, J., Guilderson, T., Adkins, J., Sarnthein, M., Baker, L., Yarusinsky, M., 2000.
855 Abrupt onset and termination of the African Humid Period: Rapid climate responses to
856 gradual insolation forcing. *Quaternary Science Reviews* 19, 347–361.
857 [https://doi.org/10.1016/S0277-3791\(99\)00081-5](https://doi.org/10.1016/S0277-3791(99)00081-5)
858 Dosseto, A., Vigier, N., Joannes-Boyau, R., Moffat, I., Singh, T., Srivastava, P., 2015. Rapid response of
859 silicate weathering rates to climate change in the Himalaya. *Geochemical Perspectives*
860 *Letters* 10–19. <https://doi.org/10.7185/geochemlet.1502>

861 Ducassou, E., Migeon, S., Mulder, T., Murat, A., Capotondi, L., Bernasconi, S.M., Mascle, J., 2009.
862 Evolution of the Nile deep-sea turbidite system during the late Quaternary: Influence of
863 climate change on fan sedimentation. *Sedimentology* 56, 2061–2090.
864 <https://doi.org/10.1111/j.1365-3091.2009.01070.x>

865 Ducassou, E., Mulder, T., Migeon, S., Gonthier, E., Murat, A., Revel, M., Capotondi, L., Bernasconi,
866 S.M., Mascle, J., Zaragosi, S., 2008. Nile floods recorded in deep Mediterranean sediments.
867 *Quaternary Research* 70, 382–391. <https://doi.org/10.1016/j.yqres.2008.02.011>

868 Dupont, L.M., Jahns, S., Marret, F., Ning, S., 2000. Vegetation change in equatorial West Africa: time-
869 slices for the last 150 ka. *Palaeogeography, Palaeoclimatology, Palaeoecology* 155, 95–122.
870 [https://doi.org/10.1016/S0031-0182\(99\)00095-4](https://doi.org/10.1016/S0031-0182(99)00095-4)

871 Dupuis, R., Benoit, M., Tuckerman, M.E., Méheut, M., 2017. Importance of a Fully Anharmonic
872 Treatment of Equilibrium Isotope Fractionation Properties of Dissolved Ionic Species As
873 Evidenced by Li+(aq). *Accounts of Chemical Research* 50, 1597–1605.
874 <https://doi.org/10.1021/acs.accounts.6b00607>

875 Ehrmann, W., Schmiedl, G., Beuscher, S., Krüger, S., 2017. Intensity of African Humid Periods
876 Estimated from Saharan Dust Fluxes. *PLOS ONE* 12, e0170989.
877 <https://doi.org/10.1371/journal.pone.0170989>

878 Emeis, K.-C., Schulz, H., Struck, U., Rossignol-Strick, M., Erlenkeuser, H., Howell, M.W., Kroon, D.,
879 Mackensen, A., Ishizuka, S., Oba, T., Sakamoto, T., Koizumi, I., 2003. Eastern Mediterranean
880 surface water temperatures and $\delta^{18}\text{O}$ composition during deposition of sapropels in the late
881 Quaternary: SST AND $\delta^{18}\text{O}$ OF MEDITERRANEAN SAPROPELS. *Paleoceanography* 18, n/a-n/a.
882 <https://doi.org/10.1029/2000PA000617>

883 Faccenna, C., Glišović, P., Forte, A., Becker, T.W., Garzanti, E., Sembroni, A., Gvirtzman, Z., 2019. Role
884 of dynamic topography in sustaining the Nile River over 30 million years. *Nat. Geosci.*
885 <https://doi.org/10.1038/s41561-019-0472-x>

886 Fielding, L., Najman, Y., Millar, I., Butterworth, P., Ando, S., Padoan, M., Barfod, D., Kneller, B., 2017.
887 A detrital record of the Nile River and its catchment. *Journal of the Geological Society* 174,
888 301–317. <https://doi.org/10.1144/jgs2016-075>

889 Foerster, V., Junginger, A., Langkamp, O., Gebru, T., Asrat, A., Umer, M., Lamb, H.F., Wennrich, V.,
890 Rethemeyer, J., Nowaczyk, N., Trauth, M.H., Schaebitz, F., 2012. Climatic change recorded in
891 the sediments of the Chew Bahir basin, southern Ethiopia, during the last 45,000 years.
892 *Quaternary International* 274, 25–37. <https://doi.org/10.1016/j.quaint.2012.06.028>

893 Garcin, Y., Vincens, A., Williamson, D., Buchet, G., Guiot, J., 2007. Abrupt resumption of the African
894 Monsoon at the Younger Dryas-Holocene climatic transition. *Quaternary Science Reviews* 26,
895 690–704. <https://doi.org/10.1016/j.quascirev.2006.10.014>

896 Garzanti, E., Andò, S., Padoan, M., Vezzoli, G., El Kammar, A., 2015a. The modern Nile sediment
897 system: Processes and products. *Quaternary Science Reviews* 130, 9–56.
898 <https://doi.org/10.1016/j.quascirev.2015.07.011>

899 Garzanti, E., Andò, S., Padoan, M., Vezzoli, G., El Kammar, A., 2015b. The modern Nile sediment
900 system: Processes and products. *Quaternary Science Reviews* 130, 9–56.
901 <https://doi.org/10.1016/j.quascirev.2015.07.011>

902 Gasse, F., 2000. Hydrological changes in the African tropics since the Last Glacial Maximum.
903 *Quaternary Science Reviews* 19, 189–211.

904 Ghilardi, M., Boraik, M., 2011. Reconstructing the Holocene depositional environments in the
905 western part of Ancient Karnak temples complex (Egypt): A geoarchaeological approach.
906 *Journal of Archaeological Science* 38, 3204–3216. <https://doi.org/10.1016/j.jas.2011.06.007>

907 Grousset, F.E., Biscaye, P.E., 2005. Tracing dust sources and transport patterns using Sr, Nd and Pb
908 isotopes. *Chemical Geology* 222, 149–167. <https://doi.org/10.1016/j.chemgeo.2005.05.006>

909 Grousset, F.E., Biscaye, P.E., Zindler, A., Prospero, J., Chester, R., 1988. Neodymium Isotopes As
910 Tracers in Marine-Sediments and Aerosols - North-Atlantic. *Earth and Planetary Science*
911 *Letters* 87, 367–378. [https://doi.org/10.1016/0012-821x\(88\)90001-5](https://doi.org/10.1016/0012-821x(88)90001-5)

912 Hamann, Y., Ehrmann, W., Schmiedl, G., Kuhnt, T., 2009. Modern and late Quaternary clay mineral
913 distribution in the area of the SE Mediterranean Sea. *Quaternary Research* 71, 453–464.
914 <https://doi.org/10.1016/j.yqres.2009.01.001>

915 Heinrich, Hartmut, 1988. Origin and Consequences of Cyclic Ice Rafting in the Northeast Atlantic
916 Ocean During the Past 130,000 Years. *Quat. res.* 29, 142–152. [https://doi.org/10.1016/0033-5894\(88\)90057-9](https://doi.org/10.1016/0033-5894(88)90057-9)
917

918 Heinrich, H, 1988. Origin and Consequences of Cyclic Ice Rafting in the Northeast Atlantic-Ocean
919 During the Past 130,000 Years. *Quaternary Research* 29, 142–152.
920 [https://doi.org/10.1016/0033-5894\(88\)90057-9](https://doi.org/10.1016/0033-5894(88)90057-9)

921 Heinrich, H., Schmidt, C., Ziemer, F., Mikolajewicz, U., Roettig, C.-B., 2021. Massive deposition of
922 Sahelian dust on the Canary Island Lanzarote during North Atlantic Heinrich Events. *Quat.*
923 *res.* 1–16. <https://doi.org/10.1017/qua.2020.100>

924 Hemming, S.R., 2004. Heinrich events: Massive late Pleistocene detritus layers of the North Atlantic
925 and their global climate imprint. *Reviews of Geophysics* 42, 1–43.
926 <https://doi.org/10.1029/2003RG000128.1>.INTRODUCTION

927 Hennekam, R., Donders, T.H., Zwiep, K., de Lange, G.J., 2015. Integral view of Holocene precipitation
928 and vegetation changes in the Nile catchment area as inferred from its delta sediments.
929 *Quaternary Science Reviews* 130, 189–199. <https://doi.org/10.1016/j.quascirev.2015.05.031>

930 Hijmans, R.J., Cameron, S.E., Parra, J.L., Jones, G., Jarvis, A., 2005. Very high resolution interpolated
931 Climate surfaces for Global land areas. *International Journal of Climatology* 25, 1965–1978.
932 <https://doi.org/10.1002/joc.1276>

933 Huh, Y., Chan, L.-H., Zhang, L., Edmond, J.M., 1998. Lithium and its isotopes in major world rivers:
934 implications for weathering and the oceanic budget. *Geochimica et Cosmochimica Acta* 62,
935 2039–2051. [https://doi.org/10.1016/S0016-7037\(98\)00126-4](https://doi.org/10.1016/S0016-7037(98)00126-4)

936 Johnson, P.R., Andresen, A., Collins, A.S., Fowler, A.R., Fritz, H., Ghebreab, W., Kusky, T., Stern, R.J.,
937 2011. Late Cryogenian–Ediacaran history of the Arabian–Nubian Shield: A review of
938 depositional, plutonic, structural, and tectonic events in the closing stages of the northern
939 East African Orogen. *Journal of African Earth Sciences* 61, 167–232.
940 <https://doi.org/10.1016/j.jafrearsci.2011.07.003>

941 Johnson, T.C., Malala, J.O., 2009. Lake Turkana and Its Link to the Nile, in: Dumont, H.J. (Ed.), *The*
942 *Nile, Monographiae Biologicae*. Springer Netherlands, Dordrecht, pp. 287–304.
943 https://doi.org/10.1007/978-1-4020-9726-3_15

944 Kallel, N., Duplessy, J.C., Labeyrie, L., Fontugne, M., Paterne, M., Montacer, M., 2000. Mediterranean
945 pluvial periods and sapropel formation over the last 200 000 years. *Palaeogeography,*
946 *Palaeoclimatology, Palaeoecology* 157, 45–58. [https://doi.org/10.1016/S0031-0182\(99\)00149-2](https://doi.org/10.1016/S0031-0182(99)00149-2)
947

948 Kelly, M.A., Russell, J.M., Baber, M.B., Howley, J.A., Loomis, S.E., Zimmerman, S., Nakileza, B., Lukaye,
949 J., 2014. Expanded glaciers during a dry and cold Last Glacial Maximum in equatorial East
950 Africa. *Geology* 42, 519–522. <https://doi.org/10.1130/G35421E.1>

951 Krom, M.D., Cliff, R.A., Eijsink, L.M., Herut, B., Chester, R., 1999. The characterisation of Saharan dust
952 and Nile particulate matter in surface sediments from the Levantine basin using Sr isotopes.
953 *Marine Geology* 155, 319–330.

954 Krom, M.D., Stanley, J.D., Cliff, R. a, Woodward, J.C., 2002. Nile {R}iver Sediment Fluctuation over the
955 Past 7000 yr and their Role in Sapropel Development. *Geology* 30, 71–74.
956 [https://doi.org/10.1130/0091-7613\(2002\)030<0071](https://doi.org/10.1130/0091-7613(2002)030<0071)

957 Kutzbach, J.E., Guan, J., He, F., Cohen, A.S., Orland, I.J., Chen, G., 2020. African climate response to
958 orbital and glacial forcing in 140,000-y simulation with implications for early modern human
959 environments. *Proc Natl Acad Sci USA* 117, 2255–2264.
960 <https://doi.org/10.1073/pnas.1917673117>

961 Lamb, H.F., Bates, C.R., Bryant, C.L., Davies, S.J., Huws, D.G., Marshall, M.H., Roberts, H.M., 2018.
962 150,000-year palaeoclimate record from northern Ethiopia supports early, multiple

963 dispersals of modern humans from Africa. *Scientific Reports* 8, 1–7.
964 <https://doi.org/10.1038/s41598-018-19601-w>

965 Lamb, H.F., Bates, C.R., Coombes, P. V., Marshall, M.H., Umer, M., Davies, S.J., Dejen, E., 2007. Late
966 Pleistocene desiccation of Lake Tana, source of the Blue Nile. *Quaternary Science Reviews* 26,
967 287–299. <https://doi.org/10.1016/j.quascirev.2006.11.020>

968 Langgut, D., Almogi-Labin, A., Bar-Matthews, M., Weinstein-Evron, M., 2011. Vegetation and climate
969 changes in the South Eastern Mediterranean during the Last Glacial-Interglacial cycle (86 ka):
970 New marine pollen record. *Quaternary Science Reviews* 30, 3960–3972.
971 <https://doi.org/10.1016/j.quascirev.2011.10.016>

972 Le Quilleuc, M., A., Bory, A., Philippe, S., Derimian, Y., Skonieczny, C., Petit, J.-E., Ponlevé, D., Diallo,
973 A., Ndiaye, T., Quentin, L., Tribouvillard, N., Bout-Roumazeilles, V., submitted. Major element
974 signatures of silicate dust deposited on the West African margin: links with transport
975 patterns and provenance regions. *Journal of Geophysical Research*.

976 Li, G., West, A.J., 2014. Evolution of Cenozoic seawater lithium isotopes: Coupling of global
977 denudation regime and shifting seawater sinks. *Earth and Planetary Science Letters* 401,
978 284–293. <https://doi.org/10.1016/j.epsl.2014.06.011>

979 Limmer, D.R., Köhler, C.M., Hillier, S., Moreton, S.G., Tabrez, A.R., Clift, P.D., 2012. Chemical
980 weathering and provenance evolution of Holocene–Recent sediments from the Western
981 Indus Shelf, Northern Arabian Sea inferred from physical and mineralogical properties.
982 *Marine Geology* 326–328, 101–115. <https://doi.org/10.1016/j.margeo.2012.07.009>

983 Lisiecki, L.E., Raymo, M.E., 2005. A Pliocene-Pleistocene stack of 57 globally distributed benthic $\delta^{18}O$
984 records. *Paleoceanography* 20, 1–17. <https://doi.org/10.1029/2004PA001071>

985 Liu, X., Rendle-Birring, R., Kuhlmann, H., Li, A., 2017. Two phases of the Holocene East African
986 Humid Period: Inferred from a high-resolution geochemical record off Tanzania. *Earth and*
987 *Planetary Science Letters* 460, 123–134. <https://doi.org/10.1016/j.epsl.2016.12.016>

988 Macgregor, D.S., 2012. The development of the Nile drainage system: integration of onshore and
989 offshore evidence. *Petroleum Geoscience* 18, 417–431. <https://doi.org/10.1144/petgeo2011-074>

990

991 Marshall, M.H., Lamb, H.F., Huws, D., Davies, S.J., Bates, R., Bloemendal, J., Boyle, J., Leng, M.J.,
992 Umer, M., Bryant, C., 2011. Late Pleistocene and Holocene drought events at Lake Tana, the
993 source of the Blue Nile. *Global and Planetary Change* 78, 147–161.
994 <https://doi.org/10.1016/j.gloplacha.2011.06.004>

995 Martrat, B., Jimenez-Amat, P., Zahn, R., Grimalt, J.O., 2014. Similarities and dissimilarities between
996 the last two deglaciations and interglaciations in the North Atlantic region. *Quaternary*
997 *Science Reviews* 99, 122–134. <https://doi.org/10.1016/j.quascirev.2014.06.016>

998 Mascle, J., 2014. The Nile continental margin , a compendium compiled by Jean Mascle. *Marine*
999 *Geology* 358, 2017.

1000 Mcgarry, S., Bar-matthews, M., Matthews, A., 2004. Constraints on hydrological and
1001 paleotemperature variations in the Eastern Mediterranean region in the last 140 ka given by
1002 the d D values of speleothem fluid inclusions 23, 919–934.
1003 <https://doi.org/10.1016/j.quascirev.2003.06.020>

1004 McGee, D., deMenocal, P.B., Winckler, G., Stuut, J.B.W., Bradtmiller, L.I., 2013. The magnitude,
1005 timing and abruptness of changes in North African dust deposition over the last 20,000 yr.
1006 *Earth and Planetary Science Letters* 371–372, 163–176.
1007 <https://doi.org/10.1016/j.epsl.2013.03.054>

1008 Migeon, S., Ducassou, E., Le Gonidec, Y., Rouillard, P., Mascle, J., Revel-Rolland, M., 2010. Lobe
1009 construction and sand/mud segregation by turbidity currents and debris flows on the
1010 western Nile deep-sea fan (Eastern Mediterranean). *Sedimentary Geology* 229, 124–143.
1011 <https://doi.org/10.1016/j.sedgeo.2010.02.011>

1012 Millot, R., Guerrot, C., Vigier, N., 2004. Accurate and high-precision measurement of lithium isotopes
1013 in two reference materials by MC-ICP-MS. *Geostandards and Geoanalytical Research* 28,
1014 153–159. <https://doi.org/10.1111/j.1751-908X.2004.tb01052.x>

1015 Misra, S., Froelich, P.N., 2012. Lithium Isotope History of Cenozoic Seawater: Changes in Silicate
1016 Weathering and Reverse Weathering. *Science* 335, 818–823.
1017 <https://doi.org/10.1126/science.1214697>

1018 Mohtadi, M., Prange, M., Steinke, S., 2016. Palaeoclimatic insights into forcing and response of
1019 monsoon rainfall. *Nature* 533, 191–199. <https://doi.org/10.1038/nature17450>

1020 Mollieux, S., Kettner, A.J., Laurent, D., Droz, L., Marsset, T., Laraque, A., Rabineau, M., Moukandi
1021 N’Kaya, G.D., 2019. Simulating sediment supply from the Congo watershed over the last 155
1022 ka Simulating sediment supply from the Congo watershed over the last 155 ka . Keywords.
1023 *Quaternary Science Reviews* 203, 38–55. <https://doi.org/10.1016/j.quascirev.2018.11.001>

1024 Mologni, C., Revel, M., Blanchet, C., Bosch, D., Develle, A.-L., Orange, F., Bastian, L., Khalidi, L.,
1025 Ducassou, E., Migeon, S., 2020. Frequency of exceptional Nile flood events as an indicator of
1026 Holocene hydro-climatic changes in the Ethiopian Highlands. *Quaternary Science Reviews*
1027 247, 106543. <https://doi.org/10.1016/j.quascirev.2020.106543>

1028 Nicholson, S.E., 2000. The nature of rainfall variability over Africa on times scales of decades to
1029 millennia. *Global and Planetary Change* 26, 137–158.

1030 Padoan, M., Garzanti, E., Harlavan, Y., Villa, I.M., 2011. Tracing Nile sediment sources by Sr and Nd
1031 isotope signatures (Uganda, Ethiopia, Sudan). *Geochimica et Cosmochimica Acta* 75, 3627–
1032 3644. <https://doi.org/10.1016/j.gca.2011.03.042>

1033 Palchan, D., Stein, M., Almogi-Labin, A., Erel, Y., Goldstein, S.L., 2013. Dust transport and synoptic
1034 conditions over the Sahara–Arabia deserts during the MIS6/5 and 2/1 transitions from grain-
1035 size, chemical and isotopic properties of Red Sea cores. *Earth and Planetary Science Letters*
1036 382, 125–139. <https://doi.org/10.1016/j.epsl.2013.09.013>

1037 Pistiner, J.S., Henderson, G.M., 2003. Lithium-isotope fractionation during continental weathering
1038 processes. *Earth and Planetary Science Letters* 214, 327–339. [https://doi.org/10.1016/S0012-821X\(03\)00348-0](https://doi.org/10.1016/S0012-821X(03)00348-0)

1040 Pogge von Strandmann, Philip A.E., Vaks, A., Bar-Matthews, M., Ayalon, A., Jacob, E., Henderson,
1041 G.M., 2017. Lithium isotopes in speleothems: Temperature-controlled variation in silicate
1042 weathering during glacial cycles. *Earth and Planetary Science Letters* 469, 64–74.
1043 <https://doi.org/10.1016/j.epsl.2017.04.014>

1044 Pogge von Strandmann, Philip A. E., Vaks, A., Bar-Matthews, M., Ayalon, A., Jacob, E., Henderson,
1045 G.M., 2017. Lithium isotopes in speleothems: Temperature-controlled variation in silicate
1046 weathering during glacial cycles. *Earth and Planetary Science Letters* 469, 64–74.
1047 <https://doi.org/10.1016/j.epsl.2017.04.014>

1048 Pogge von Strandmann, P.A.E.P., Burton, K.W., James, R.H., van Calsteren, P., Gislason, S.R., 2010.
1049 Assessing the role of climate on uranium and lithium isotope behaviour in rivers draining a
1050 basaltic terrain. *Chemical Geology* 270, 227–239.
1051 <https://doi.org/10.1016/j.chemgeo.2009.12.002>

1052 Pogge von Strandmann, P.A.E.P. von, Kasemann, S.A., Wimpenny, J.B., 2020. Lithium and Lithium
1053 Isotopes in Earth’s Surface Cycles. *Elements* 16, 253–258.
1054 <https://doi.org/10.2138/gselements.16.4.253>

1055 Reimer, P.J., Edouard Bard, B., Alex Bayliss, B., Warren Beck, B.J., Paul Blackwell, B.G., Christopher
1056 Bronk Ramsey, B., 2013. Intcal13 and Marine13 Radiocarbon Age Calibration Curves 0–
1057 50,000 Years Cal Bp. *Radiocarbon* 55, 1869–1887.

1058 Revel, M., Colin, C., Bernasconi, S., Combourieu-Nebout, N., Ducassou, E., Grousset, F.E., Rolland, Y.,
1059 Migeon, S., Bosch, D., Brunet, P., Zhao, Y., Mascle, J., 2014. 21,000 Years of Ethiopian African
1060 monsoon variability recorded in sediments of the western Nile deep-sea fan. *Regional
1061 Environmental Change* 14, 1685–1696. <https://doi.org/10.1007/s10113-014-0588-x>

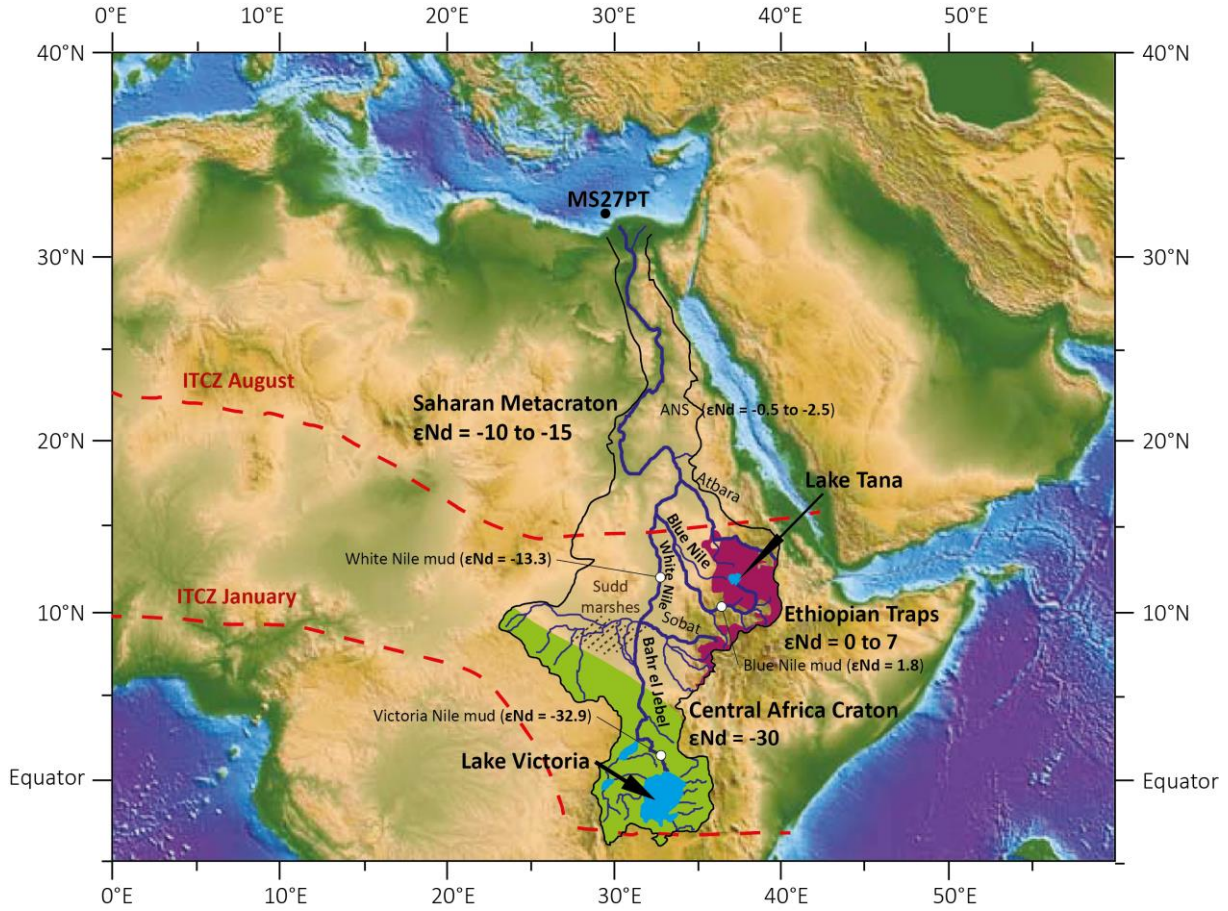
1062 Revel, M., Ducassou, E., Grousset, F.E., Bernasconi, S.M., Migeon, S., Revillon, S., Mascle, J., Murat,
1063 A., Zaragosi, S., Bosch, D., 2010. 100,000 Years of African monsoon variability recorded in
1064 sediments of the Nile margin. *Quaternary Science Reviews* 29, 1342–1362.
1065 <https://doi.org/10.1016/j.quascirev.2010.02.006>

1066 Revel, M., Ducassou, E., Skonieczny, C., Colin, C., Bastian, L., Bosch, D., Migeon, S., Mascle, J., 2015.
1067 20,000 years of Nile River dynamics and environmental changes in the Nile catchment area
1068 as inferred from Nile upper continental slope sediments. *Quaternary Science Reviews* 130.
1069 <https://doi.org/10.1016/j.quascirev.2015.10.030>
1070 Roberts, N., Taieb, M., Barker, P., Damnati, B., Icole, M., Williamson, D., 1993. Timing of the Younger
1071 Dryas event in East Africa from lake-level changes. *Nature* 366, 146–148.
1072 <https://doi.org/10.1038/366146a0>
1073 Rohling, E.J., 1994. Review and new aspects concerning the formation of eastern Mediterranean
1074 sapropel. *Marine Geochemistry* 122, 1–28.
1075 Rohling, E.J., Marino, G., Grant, K.M., 2015. Mediterranean climate and oceanography, and the
1076 periodic development of anoxic events (sapropels). *Earth-Science Reviews* 143, 62–97.
1077 <https://doi.org/10.1016/j.earscirev.2015.01.008>
1078 Rossignol-Strick, M., Nesteroff, W., Olive, P., Vergnaud-grazzini, C., 1982. After the deluge:
1079 Mediterranean stagnation and sapropel formation. *Nature* 295.
1080 Sanchez Goñi, M.F., Harrison, S.P., 2010. Millennial-scale climate variability and vegetation changes
1081 during the Last Glacial: Concepts and terminology. *Quaternary Science Reviews* 29, 2823–
1082 2827. <https://doi.org/10.1016/j.quascirev.2009.11.014>
1083 Schefuß, E., Schouten, S., Schneider, R.R., 2005. Climatic controls on central African hydrology during
1084 the past 20,000 years. *Nature* 437, 1003–1006. <https://doi.org/10.1038/nature03945>
1085 Scheuvens, D., Schütz, L., Kandler, K., Ebert, M., Weinbruch, S., 2013. Bulk composition of northern
1086 African dust and its source sediments — A compilation. *Earth-Science Reviews* 116, 170–194.
1087 <https://doi.org/10.1016/j.earscirev.2012.08.005>
1088 Shanahan, T.M., McKay, N.P., Hughen, K.A., Overpeck, J.T., Otto-Bliesner, B., Heil, C.W., King, J.,
1089 Scholz, C.A., Peck, J., 2015. The time-transgressive termination of the African humid period.
1090 *Nature Geoscience* 8, 140–144. <https://doi.org/10.1038/ngeo2329>
1091 Singarayer, J.S., Burrough, S.L., 2015. Interhemispheric dynamics of the African rainbelt during the
1092 late Quaternary. *Quaternary Science Reviews* 124, 48–67.
1093 <https://doi.org/10.1016/j.quascirev.2015.06.021>
1094 Skonieczny, C., Mcgee, D., Winckler, G., Bory, A., Bradtmiller, L.I., Kinsley, C.W., 2019. Monsoon-
1095 driven Saharan dust variability over the past 240, 000 years. *Science* 5, 1–9.
1096 Skonieczny, C., Paillou, P., Bory, A., Bayon, G., Biscara, L., Crosta, X., Eynaud, F., Malaizé, B., Revel, M.,
1097 Aleman, N., Barusseau, J.P., Vernet, R., Lopez, S., Grousset, F., 2015. African humid periods
1098 triggered the reactivation of a large river system in Western Sahara. *Nature Communications*
1099 6. <https://doi.org/10.1038/ncomms9751>
1100 Snoeckx, H., Grousset, F., Revel, M., Boelaert, A., 1999. European contribution of ice-rafted sand to
1101 Heinrich layers H3 and H4. *Marine Geology* 158, 197–208. [https://doi.org/10.1016/S0025-3227\(98\)00168-6](https://doi.org/10.1016/S0025-3227(98)00168-6)
1102
1103 Stager, J.C., Johnson, T.C., 2008. The late Pleistocene desiccation of Lake Victoria and the origin of its
1104 endemic biota. *Hydrobiologia* 596, 5–16. <https://doi.org/10.1007/s10750-007-9158-2>
1105 Talbot, M.R., Brendeland, K.I., 2001. Strontium Isotopes as Palaeohydrological Tracers in the White
1106 Nile Headwater Lakes, East Africa. *AGU Fall Meeting Abstracts* 21, PP21C-05.
1107 Talbot, M.R., Lærdal, T., 2000. The Late Pleistocene - Holocene palaeolimnology of Lake Victoria, East
1108 Africa, based upon elemental and isotopic analyses of sedimentary organic matter. *Journal of*
1109 *Paleolimnology* 23, 141–164. <https://doi.org/10.1023/A:1008029400463>
1110 Tanaka, T., Togashi, S., Kamioka, H., Amakawa, H., Kagami, H., Hamamoto, T., Yuhara, M., Orihashi,
1111 Y., Yoneda, S., Shimizu, H., Kunimaru, T., Takahashi, K., Yanagi, T., Nakano, T., Fujimaki, H.,
1112 Shinjo, R., Asahara, Y., Tanimizu, M., Dragusanu, C., 2000. JNdi-1: A neodymium isotopic
1113 reference in consistency with LaJolla neodymium. *Chemical Geology* 168, 279–281.
1114 [https://doi.org/10.1016/S0009-2541\(00\)00198-4](https://doi.org/10.1016/S0009-2541(00)00198-4)
1115 Tierney, J.E., DeMenocal, P.B., 2013. Abrupt Shifts in Horn of Africa Since the Last Glacial Maximum.
1116 *Science* 342, 843–846. <https://doi.org/10.1126/science.1240411>

1117 Tierney, J.E., Lewis, S.C., Cook, B.I., LeGrande, A.N., Schmidt, G.A., 2011a. Model, proxy and isotopic
1118 perspectives on the East African Humid Period. *Earth and Planetary Science Letters* 307, 103–
1119 112. <https://doi.org/10.1016/j.epsl.2011.04.038>
1120 Tierney, J.E., Pausata, F.S.R., De Menocal, P.B., 2017. Rainfall regimes of the Green Sahara. *Science*
1121 *Advances* 3, 1–10. <https://doi.org/10.1126/sciadv.1601503>
1122 Tierney, J.E., Russell, J.M., Huang, Y., Sinninghe Damsté, J.S., Hopmans, E.C., Cohen, A.S., 2008.
1123 Northern hemisphere controls on tropical southeast African climate during the past 60,000
1124 years. *Science* 322, 252–255. <https://doi.org/10.1126/science.1160485>
1125 Tierney, J.E., Russell, J.M., Sinninghe Damsté, J.S., Huang, Y., Verschuren, D., 2011b. Late Quaternary
1126 behavior of the East African monsoon and the importance of the Congo Air Boundary.
1127 *Quaternary Science Reviews* 30, 798–807. <https://doi.org/10.1016/j.quascirev.2011.01.017>
1128 Tierney, J.E., Smerdon, J.E., Anchukaitis, K.J., Seager, R., 2013. Multidecadal variability in East African
1129 hydroclimate controlled by the Indian Ocean. *Nature* 493, 389–392.
1130 <https://doi.org/10.1038/nature11785>
1131 Tjallingii, R., Claussen, M., Stuut, J.-B.W., Fohlmeister, J., Jahn, A., Bickert, T., Lamy, F., Röhl, U., 2008.
1132 Coherent high- and low-latitude control of the northwest African hydrological balance.
1133 *Nature Geosci* 1, 670–675. <https://doi.org/10.1038/ngeo289>
1134 Verschuren, D., Russell, J.M., 2009. Paleolimnology of African lakes : Beyond the exploration phase.
1135 *PAGES news* 17, 112–114. <https://doi.org/10.1029/2008JD010145>.Yancheva
1136 Verschuren, D., Sinninghe Damsté, J.S., Moernaut, J., Kristen, I., Blaauw, M., Fagot, M., Haug, G.H.,
1137 2009. Half-precessional dynamics of monsoon rainfall near the East African Equator. *Nature*
1138 462, 637–641. <https://doi.org/10.1038/nature08520>
1139 Vigier, N., Decarreau, A., Millot, R., Carignan, J., Petit, S., France-Lanord, C., 2008. Quantifying Li
1140 isotope fractionation during smectite formation and implications for the Li cycle. *Geochimica*
1141 *et Cosmochimica Acta* 72, 780–792. <https://doi.org/10.1016/j.gca.2007.11.011>
1142 Vigier, N., Gislason, S.R., Burton, K.W., Millot, R., Mokadem, F., 2009. The relationship between
1143 riverine lithium isotope composition and silicate weathering rates in Iceland. *Earth and*
1144 *Planetary Science Letters* 287, 434–441. <https://doi.org/10.1016/j.epsl.2009.08.026>
1145 Viste, E., Sorteberg, A., 2013. The effect of moisture transport variability on Ethiopian summer
1146 precipitation. *International Journal of Climatology* 33, 3106–3123.
1147 <https://doi.org/10.1002/joc.3566>
1148 Waelbroeck, C., Pichat, S., Böhm, E., Lougheed, B.C., Faranda, D., Vrac, M., Missiaen, L., Vazquez
1149 Riveiros, N., Burckel, P., Lippold, J., Arz, H.W., Dokken, T., Thil, F., Dapoigny, A., 2018. Relative
1150 timing of precipitation and ocean circulation changes in the western equatorial Atlantic over
1151 the last 45 kyr. *Clim. Past* 14, 1315–1330. <https://doi.org/10.5194/cp-14-1315-2018>
1152 Wang, Y., Cheng, H., Edwards, R.L., Kong, X., Shao, X., Chen, S., Wu, J., Jiang, X., Wang, X., An, Z.,
1153 2008. Millennial- and orbital-scale changes in the East Asian monsoon over the past 224,000
1154 years. *Nature* 451, 1090–1093. <https://doi.org/10.1038/nature06692>
1155 Weldeab, S., Emeis, K.C., Hemleben, C., Schmiedl, G., Schulz, H., 2003. Spatial productivity variations
1156 during formation of sapropels S5 and S6 in the Mediterranean Sea: Evidence from Ba
1157 contents. *Palaeogeography, Palaeoclimatology, Palaeoecology* 191, 169–190.
1158 [https://doi.org/10.1016/S0031-0182\(02\)00711-3](https://doi.org/10.1016/S0031-0182(02)00711-3)
1159 Weldeab, S., Menke, V., Schmiedl, G., 2014. The pace of East African monsoon evolution during the
1160 Holocene. *Geophysical Research Letters* 41, 1724–1731.
1161 <https://doi.org/10.1002/2014GL059361>.Received
1162 Williams, M., 2019. *The Nile Basin: Quaternary Geology, Geomorphology and Prehistoric*
1163 *Environments*, 1st ed. Cambridge University Press. <https://doi.org/10.1017/9781316831885>
1164 Williams, M., Talbot, M., Aharon, P., Abdl Salaam, Y., Williams, F., Inge Brendeland, K., 2006. Abrupt
1165 return of the summer monsoon 15,000 years ago: new supporting evidence from the lower
1166 White Nile valley and Lake Albert. *Quaternary Science Reviews* 25, 2651–2665.
1167 <https://doi.org/10.1016/j.quascirev.2005.07.019>

- 1168 Williams, M.A.J., Usai, D., Salvatori, S., Williams, F.M., Zerboni, A., Maritan, L., Linseele, V., 2015. Late
1169 Quaternary environments and prehistoric occupation in the lower White Nile valley, central
1170 Sudan. *Quaternary Science Reviews* 130, 72–88.
1171 <https://doi.org/10.1016/j.quascirev.2015.03.007>
- 1172 Williams, M.A.J., Williams, F.M., Duller, G.A.T., Munro, R.N., El Tom, O.A.M., Barrows, T.T., Macklin,
1173 M., Woodward, J., Talbot, M.R., Haberlah, D., 2010. Late Quaternary floods and droughts in
1174 the Nile valley, Sudan: new evidence from optically stimulated luminescence and AMS
1175 radiocarbon dating. *Quaternary Science Reviews* 29, 1116–1137.
1176 <https://doi.org/10.1016/j.quascirev.2010.02.018>
- 1177 Wimpenny, J., Gíslason, S.R., James, R.H., Gannoun, A., Pogge Von Strandmann, P.A.E., Burton, K.W.,
1178 2010. The behaviour of Li and Mg isotopes during primary phase dissolution and secondary
1179 mineral formation in basalt. *Geochimica et Cosmochimica Acta* 74, 5259–5279.
1180 <https://doi.org/10.1016/j.gca.2010.06.028>
- 1181 Woodward, J., Macklin, M., Fielding, L., Millar, I., Spencer, N., Welsby, D., Williams, M., 2015. Shifting
1182 sediment sources in the world’s longest river: A strontium isotope record for the Holocene
1183 Nile. *Quaternary Science Reviews* 130, 124–140.
1184 <https://doi.org/10.1016/j.quascirev.2015.10.040>
- 1185 Ziegler, M., Tuenter, E., Lourens, L.J., 2010. The precession phase of the boreal summer monsoon as
1186 viewed from the eastern Mediterranean (ODP Site 968). *Quaternary Science Reviews* 29,
1187 1481–1490. <https://doi.org/10.1016/j.quascirev.2010.03.011>
1188
- 1189

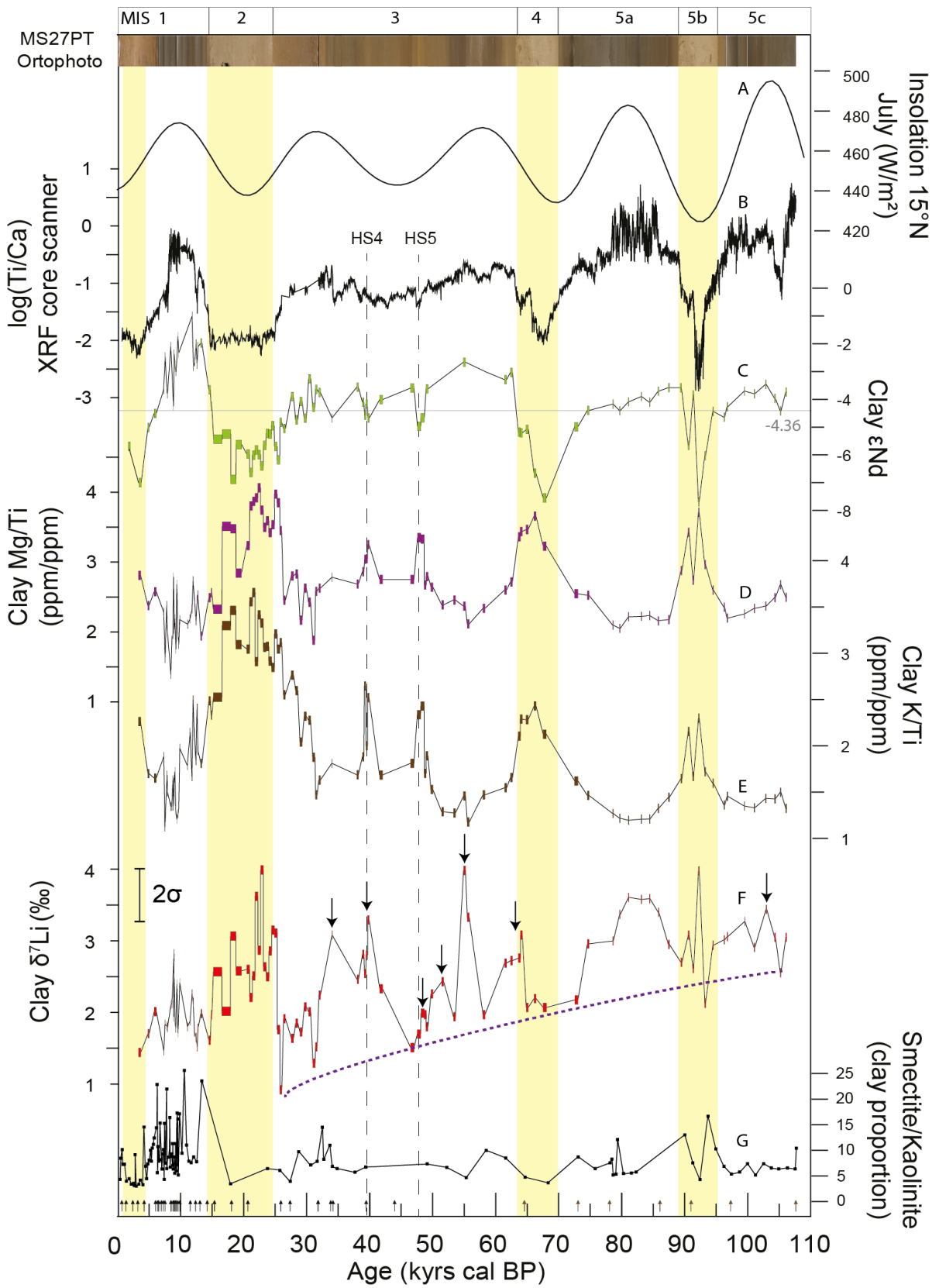
1190



1191

1192 *Figure 1 : Map of the Nile River basin and location of core MS27PT (N31°47.90'; E29°27.70', 1389 m*
1193 *m water deep). Three main sources of suspended sediment load are identified in the Nile basin: the*
1194 *basaltic rocks (purple) of the Ethiopian Traps (Highlands), which are drained by the Blue Nile, the*
1195 *Atbara and Sobat rivers located in tropical latitude (around 5 to 15°N); The Precambrian*
1196 *metamorphic rocks (green) of the Central African Craton located in the equatorial latitude of the lakes*
1197 *Albert and Victoria in the Ugandan headwaters region of the White Nile, which are drained by the*
1198 *Bahr el Jebel River; and the Saharan Metacraton sources (Abdelsalam et al., 2002; Grousset and*
1199 *Biscaye, 2005; Scheuvens et al., 2013). ϵNd of the Victoria, White and Blue Nile River mud samples are*
1200 *from Garzanti et al., (2015). ANS: Arabian-Nubian Shield (ϵNd from Palchan et al., 2013).*

1201



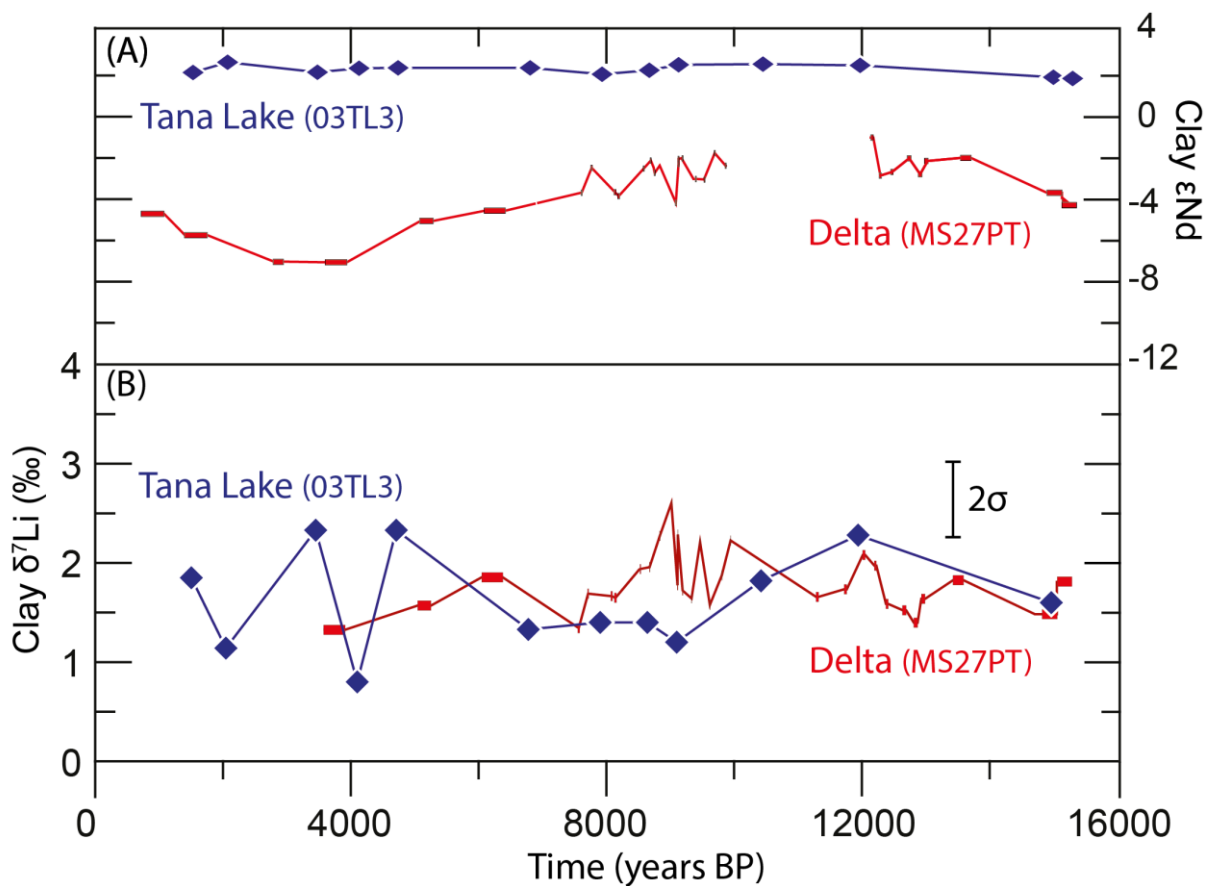
1203

1204 *Figure 2 : Paleo-variations in (A) July insolation at 15°N (Berger and Loutre, 1991), (B) log(Ti/Ca) ratio*
 1205 *in the MS27PT bulk fraction (Revel et al., 2010) , (C), (D), (E), (F) and (G) clay εNd, Mg/Ti ratio, K/Ti*
 1206 *ratio, δ⁷Li and smectite/kaolinite ratio for the last 110 ka (MIS: Marine Isotopic Stage). Grey line*

1207 represent the average ϵNd value recorded over 110 ka. A photography of the MS27PT core is shown
 1208 for comparison, with the humid and arid periods characterized by dark and light sediments
 1209 respectively. The yellow bands correspond to the arid periods and dotted lines to Heinrich Stadials 4
 1210 and 5. Arrows show $\delta^7 Li$ excursion during specific short-term periods. The progressive decrease of the
 1211 $\delta^7 Li$ minima corresponds to dotted line. Black arrows refer to ^{14}C ages, brown arrows to age
 1212 calibration from the $\delta^{18}O$ of planktonic foraminifera.

1213

1214



1215

Figure 3 : Clay $\delta^7 Li$ and ϵNd as a function of the sediment age in the Lake Tana in Ethiopia (blue; core 03TL3) and for MS27PT Nile delta core downstream (red). The 2SD of the ϵNd values range between 0.08 and 0.45.

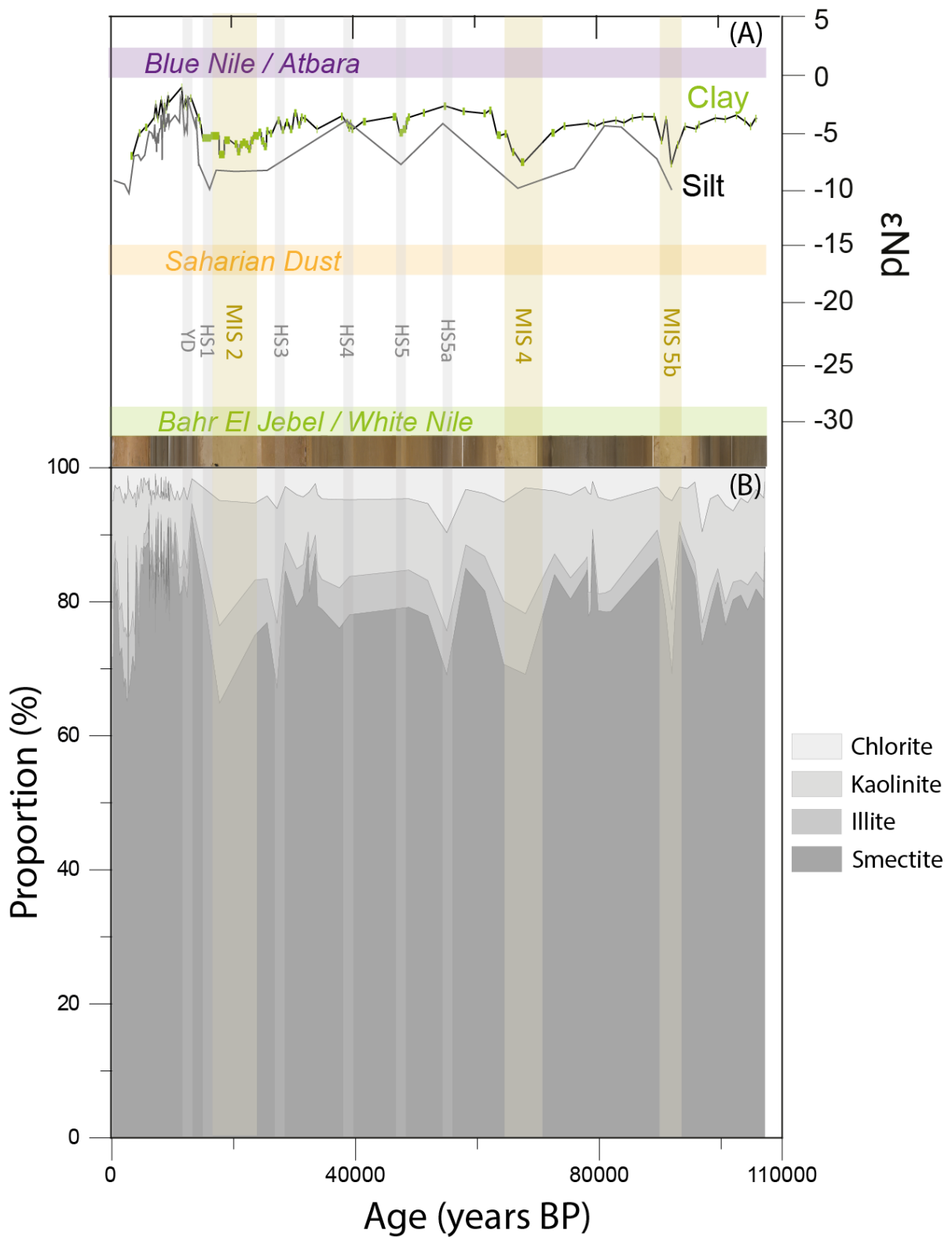


Figure 4 : (A) ϵNd values of clay fraction (green, Bastian et al., 2017) and of $<63\mu m$ fraction (grey line; Revel et al., 2010, 2015) of MS27PT sediment. (B) Percentage of clay estimated by XRD as a function of time. Light brown and grey bars indicate arid periods corresponding to MIS 2, 4, 5b and to Heinrich Stadials and younger Dryas events.

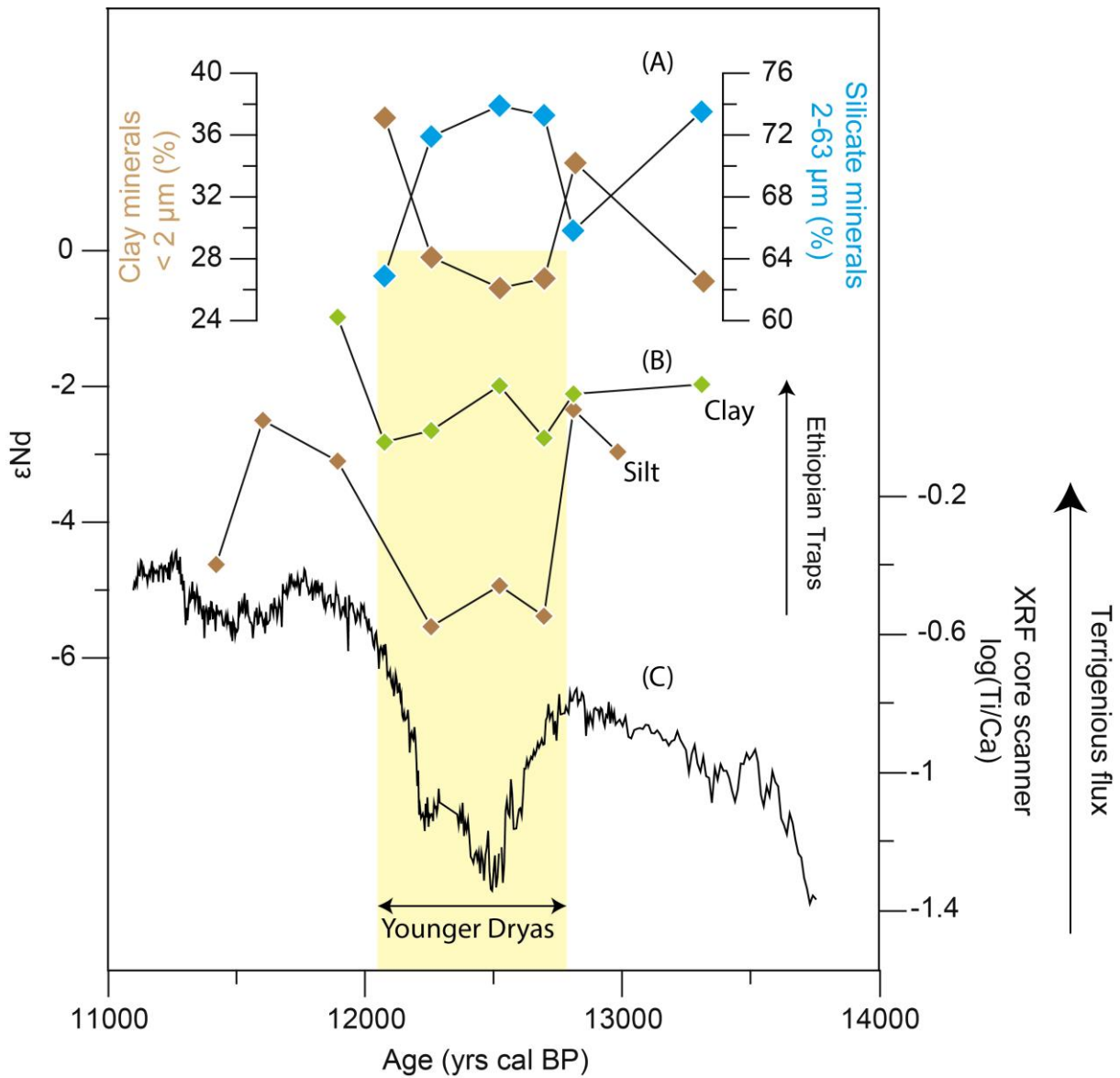
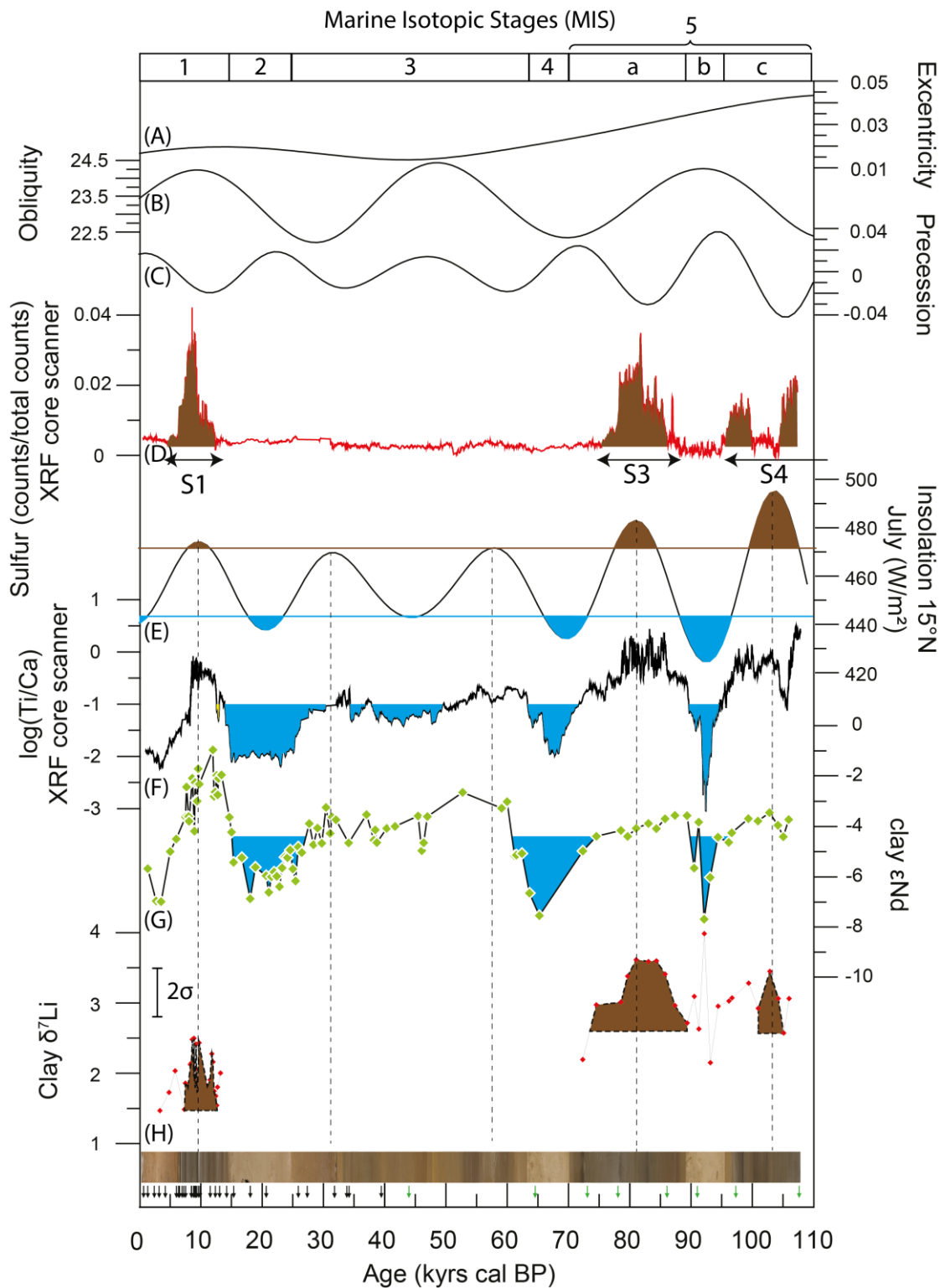


Figure 5: Paleo-variations between 11 and 14 kyrs in (A) measured minerals proportion (brown) and silicate minerals proportion (blue), (B) clay ϵ_{Nd} (green) and $<63\mu m$ fraction ϵ_{Nd} (brown, (Revel et al., 2015)) (C) $\log(Ti/Ca)$ measured by XRF core scanner (Revel et al., 2010). The 2SD of the ϵ_{Nd} range between 0.08 and 0.45.



1218

Figure 6 : Paleo-variations in (A) Eccentricity (B) Obliquity, (C) Precession, (D) Sulphur measured by XRF core scanner in core MS27PT (Revel et al., 2010), (E) insolation at 15°N in July (W/m^2) (F) $\log(Ti/Ca)$ measured by XRF core scanner in MS27PT sediment (Revel et al., 2010) (G) and (H) clay ϵNd and $\delta^7 Li$ in MS27PT sediment. The blue and brown patterns correspond respectively to the minimum and maximum insolation values for the last 110 kyrs.

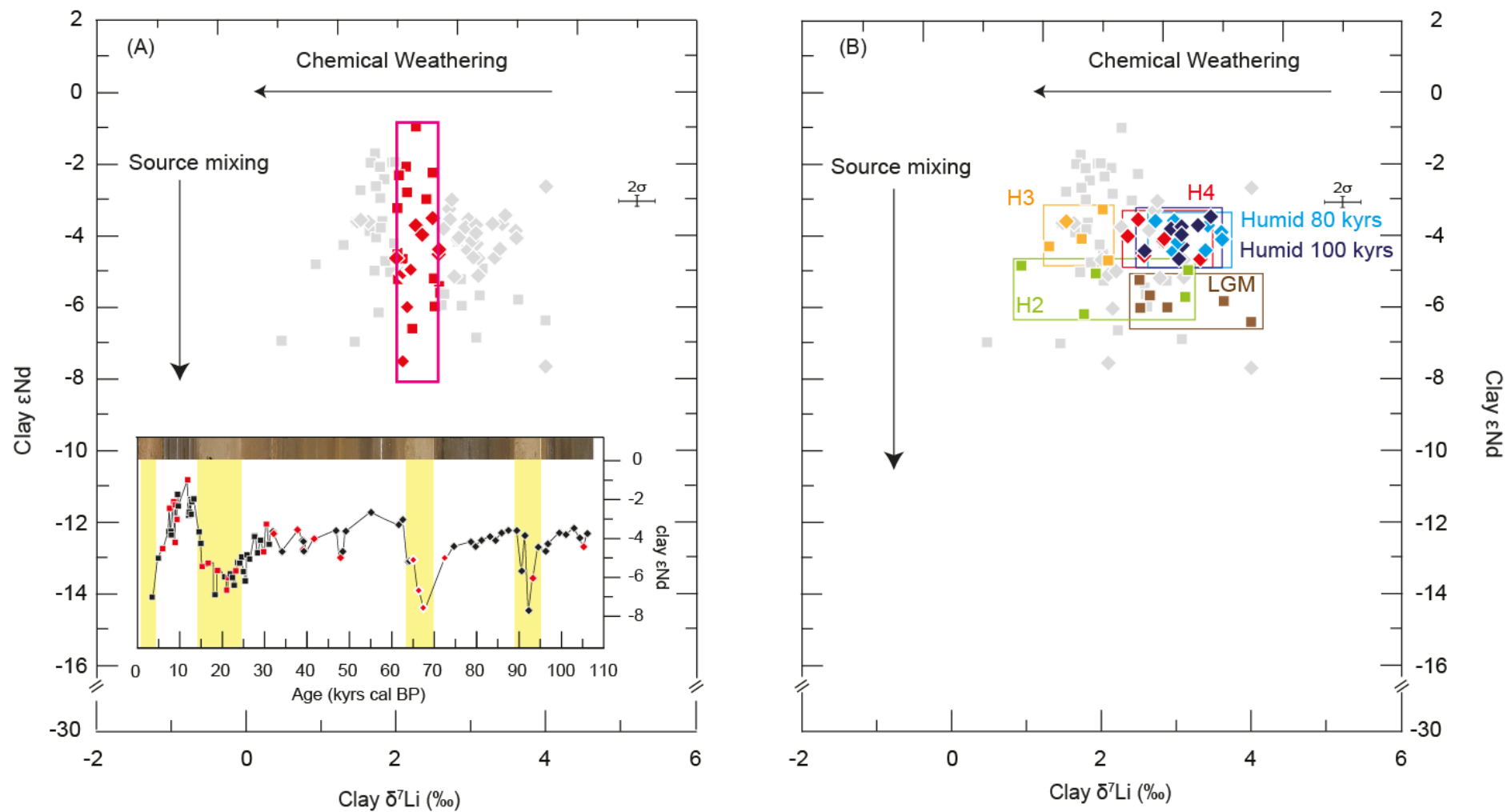
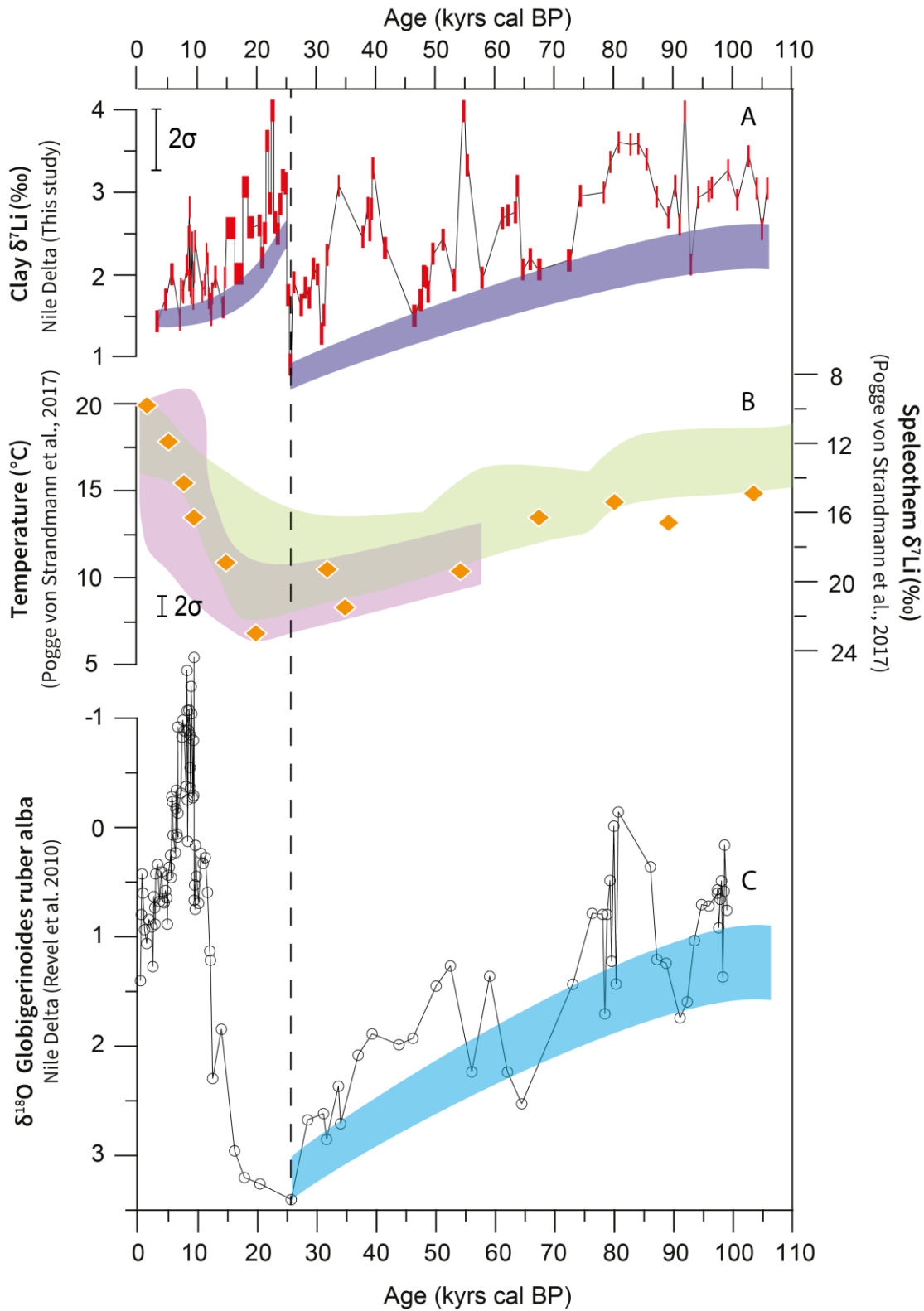


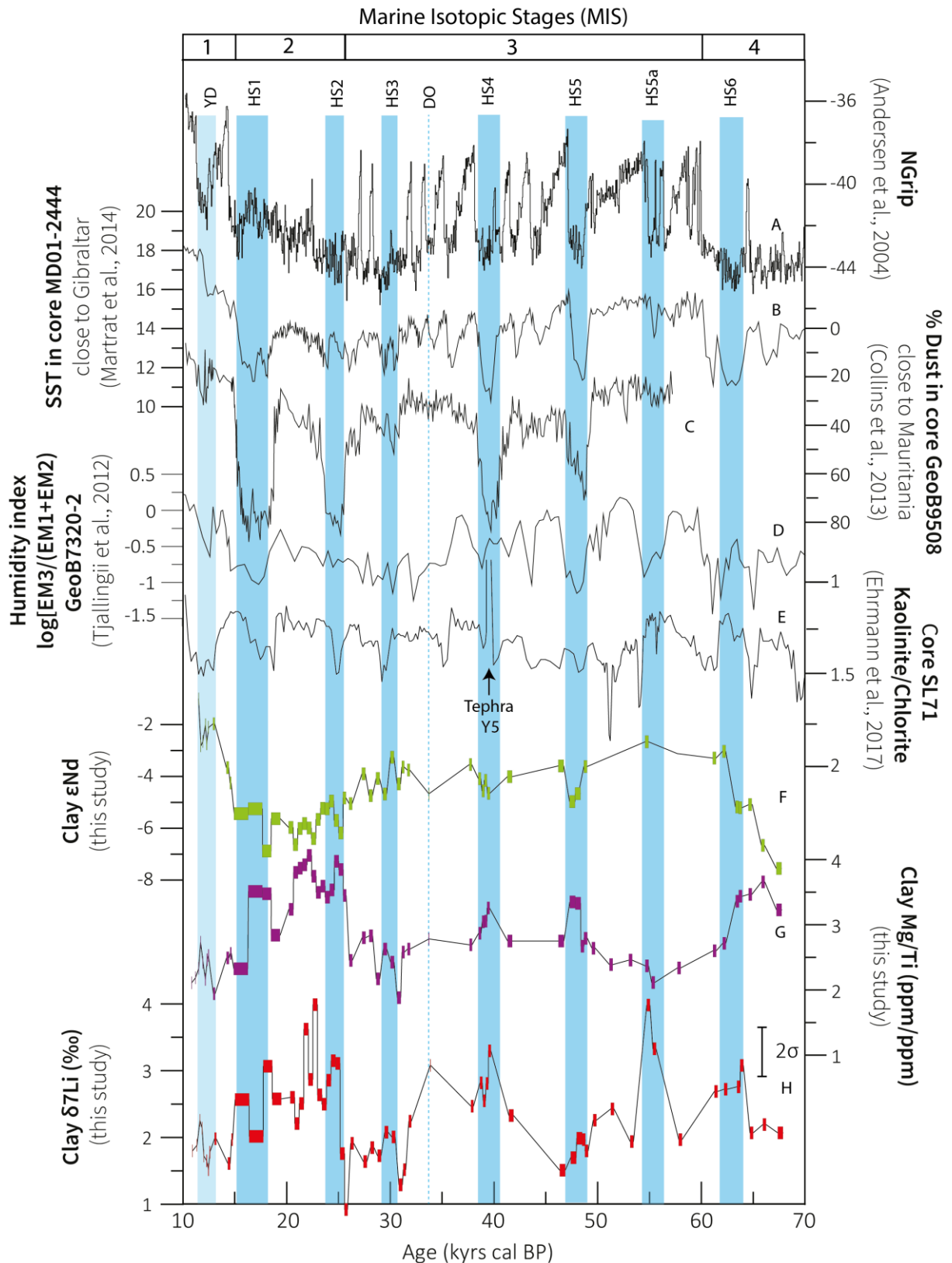
Figure 7 : Clay ϵNd as a function of $\delta^7\text{Li}$. (A) The red symbols represent samples with similar $\delta^7\text{Li}$ (≈ 2 ‰) and variable ϵNd . (B) Representation of different periods of time with constant clay ϵNd . The squares and the diamonds correspond respectively to the samples of Bastian et al., (2017) and of this study.



1220

1221 *Figure 8 : Paleovariation of (A) clay $\delta^7\text{Li}$ in core MS27PT, (B) $\delta^7\text{Li}$ in Speleothem from Soreq cave*
 1222 *(Israel). The green and violet bands correspond to the temperature reconstruction respectively with*
 1223 *hydrogen isotopes and clumped isotopes (Pogge von Strandmann et al., 2017); (C) Globigerinoides*
 1224 *ruber alba $\delta^{18}\text{O}$ in core MS27PT (Revel et al., 2010 & 2015).*

1225



1226

1227 *Figure 9 : Paleovariations in (A) NGrIP $\delta^{18}\text{O}$ (Andersen et al., 2004), (B) Reconstructed Sea Surface*
 1228 *Temperature (SST, °C) for North Atlantic (Martrat et al., 2014), (C) Estimation of Dust in core*
 1229 *GeoB9508 close to Gibraltar (Collins et al., 2013), (D) Estimation of Humidity index of central Africa*
 1230 *from the core GeoB7320-2 (Tjallingii et al., 2008), (E) Kaolinite/Chlorite ratio from SL71 core*

1231 *(Ehrmann et al., 2017), (F), (G) and (H) clay Mg/Ti ratio, clay K/Ti ratios and clay $\delta^7\text{Li}$. The blue band*
1232 *represents the Heinrich Stadial (HS) and the Younger Dryas (YD).*

1233

1234
1235
1236
1237
1238
1239
1240
1241
1242
1243
1244
1245
1246
1247
1248
1249
1250
1251
1252
1253
1254
1255
1256
1257
1258
1259
1260
1261
1262

Supplementary material

of

Co-variations of climate and silicate weathering in the Nile Basin during the Late Pleistocene

Luc Bastian^{1,2*} & Carlo Mologni^{1*†}, Nathalie Vigier², Germain Bayon³, Henry Lamb⁴,
Delphine Bosch⁵, Marie-Emmanuelle Kerros², Christophe Colin⁶, Marie Revel¹

*co-1st authors

†corresponding author: mologni@geoazur.unice.fr

¹ Université de la Cote d'Azur, CNRS, OCA, IRD, Geoazur, 250 rue Albert Einstein, 06500 Valbonne, France

² Laboratoire d'Océanographie de Villefranche sur Mer (LOV, IMEV), CNRS, Sorbonne Université, 181 chemin du Lazaret, 06320, Villefranche sur Mer, France

³ IFREMER, Unité de Recherche Géosciences Marines, 29280 Plouzané, France

⁴ Department of Geography and Earth Sciences, Aberystwyth University, Aberystwyth SY23 3 DB, UK

⁵ Géosciences Montpellier, UMR-CNRS 5243, Université de Montpellier, 34095 Montpellier, France

⁶ Laboratoire GEOsciences Paris-Sud (GEOPS), UMR 8148, CNRS-Université de Paris-Sud, Université Paris-Saclay, Bâtiment 504, 91405 Orsay Cedex, France.

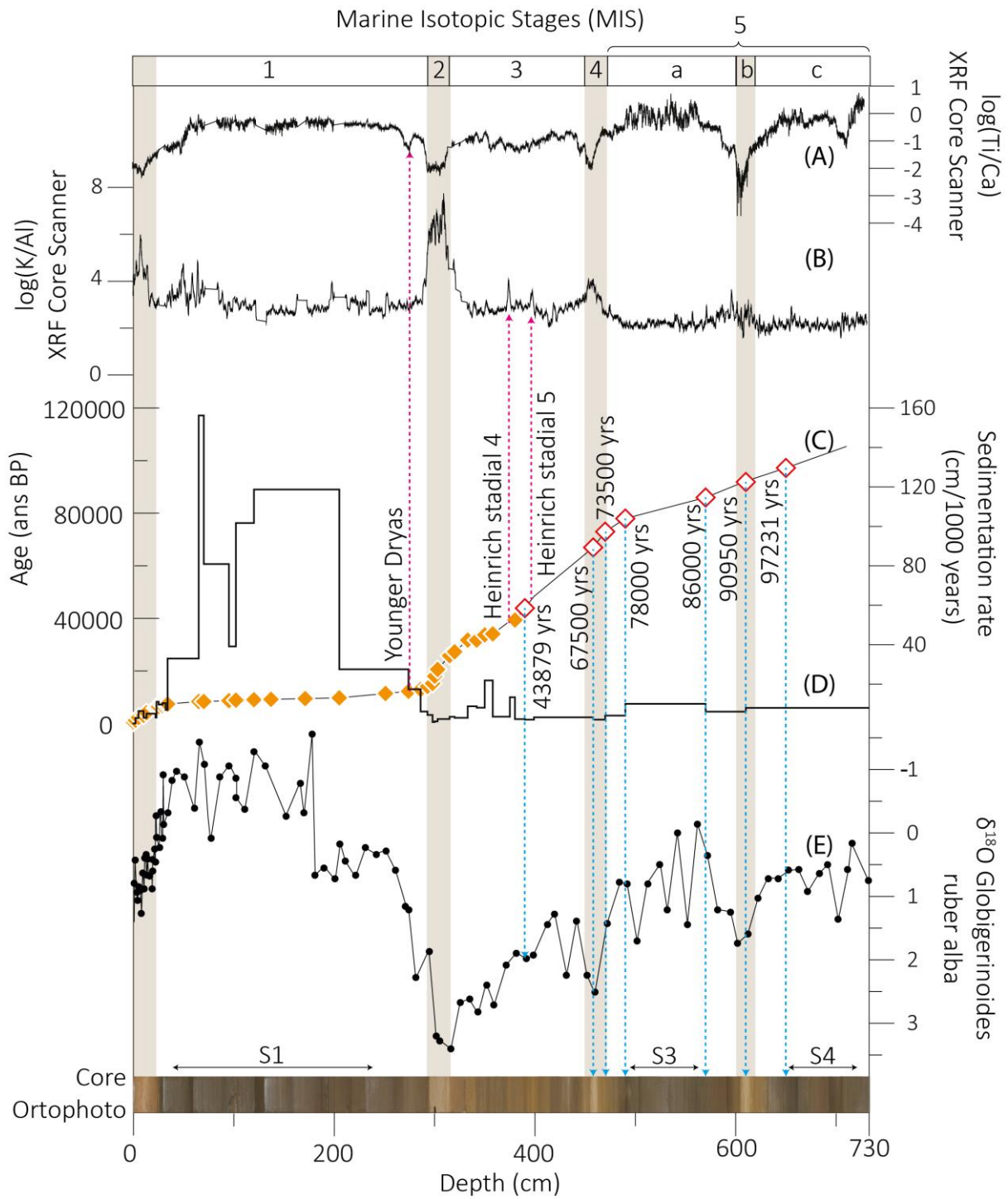
1263 Core MS27PT is 7.3 m long and cover 110 kyr. The age model for core MS27PT is based on
1264 29 AMS ¹⁴C dates first published in (Bastian et al., 2017; Revel et al., 2015, 2010). These ¹⁴C
1265 dates were calibrated using the Calib 7.0 program (Reimer et al., 2013) and a mean marine
1266 reservoir age of 400 years. For the period extending from 110 to 46 kyr BP, the age model is
1267 taken from Revel et al., (2010) and is based on the age of the sapropel S3 (86 to 78 kys BP)
1268 and the sapropel S4 (S4b: 108 kyr BP, S4a: 102 kyrs BP). Additionally, the oxygen isotope
1269 record of MS27PT is correlated with the isotope record of the SPECMAP reference timescale
1270 for the Marine Isotope Stage 4 and 5 (Cornuault et al., 2016; Kallel et al., 2000; Revel et al.,
1271 2010).

1272 The change in marine/terrigenous material and within the detrital material have been
1273 investigated by comparing the Ti/Ca and Ti/K ratios. The enrichment in Ti for humid periods
1274 indicate a higher contribution by Nile flood particles. The enrichment in K for arid periods
1275 and for some of the heinrich events most probably indicates a change in source and also a
1276 change in weathering of suspended matter. For some specific climate episodes such as the
1277 Heinrich events, we have based our sampling on K/Ti ratio variations.

1278

1279

1280



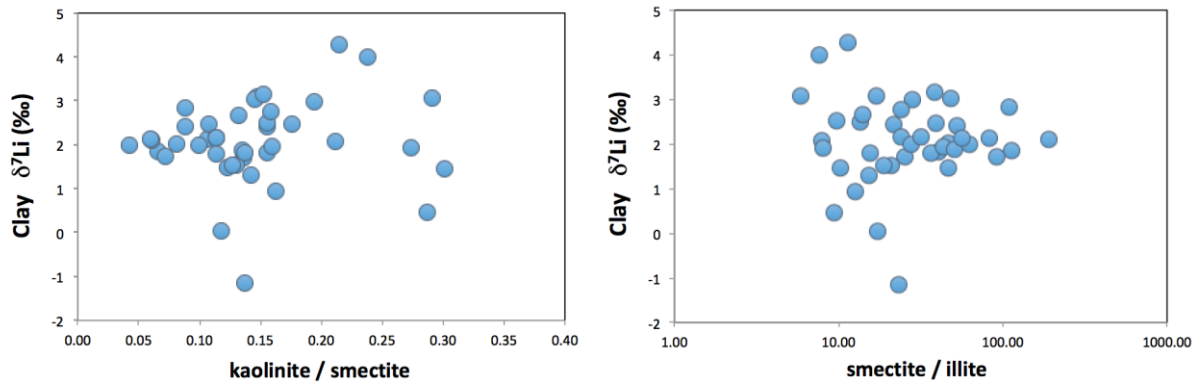
1281

Figure S1 :). (A) $\log(\text{Ti}/\text{Ca})$ determined by XRF core scanner (Revel et al., 2010). (B) K/Al determined by XRF core scanner (Revel et al., 2010) (C) AMS ^{14}C ages in orange, calibrated age in red (D) Sedimentation rate (mm/1000 years). (E) $\delta^{18}\text{O}$ of *Globigerinoides ruber alba* (Revel et al., 2010). The blue arrows indicate the age calibration after 45000 years and purple arrows indicate the Heinrich stadial 4 and 5 and Younger Dryas.

1282

1283

1284



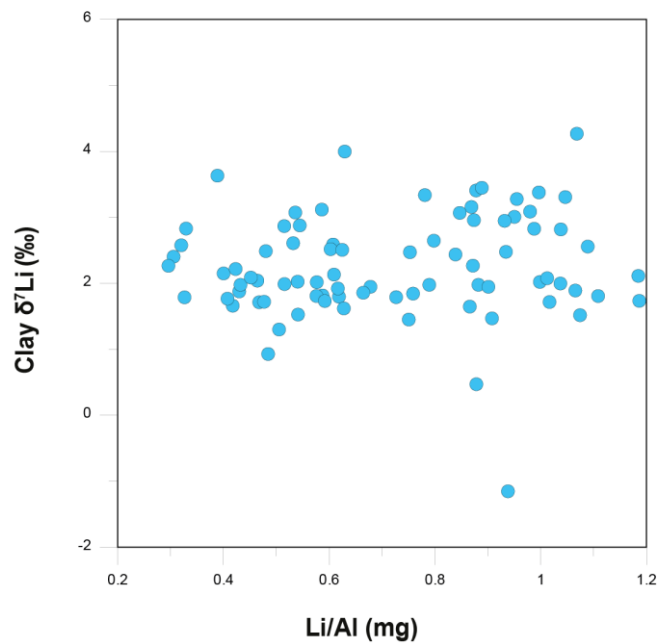
1285

1286 Figure S2: Clay $\delta^7\text{Li}$ as a function of kaolinite/smectite ratio and smectite /illite ratio. There is no
 1287 apparent correlation between clay mineralogy and clay Li isotope composition over the last 100kyrs,
 1288 mostly because smectite remained the dominant phase (>70%), and likely also because of similar
 1289 isotope fractionation during Li uptake by these various phases.

1290

1291

1292



1293

1294 *Figure S3 : Clay $\delta^7\text{Li}$ as a function of their Li/Al ratio, evidencing the lack of control by mineral mixing*
 1295 *or by significant contribution from high Li/Al – low $\delta^7\text{Li}$ shales (see Dellinger et al. 2017).*

1296